

Tectonics

RESEARCH ARTICLE

10.1029/2020TC006187

Key Points:

- Differential uplift is mapped in the Hyblean Plateau (SE Sicily, Italy) by looking at raised paleoshorelines over the Late Quaternary
- Differential uplift in the Hyblean Plateau is caused by a combined process between offshore normal faulting and regional processes
- Deformation rates associated to the offshore normal fault (Western Fault) need to be refined, subtracting the regional processes signal

Supporting Information:

- Supporting Information S1
- Data Set S1

Correspondence to:

M. Meschis,
marco.meschis.14@ucl.ac.uk

Citation:












Meschis, M., Scicchitano, G., Roberts, G. P., Robertson, J., Barreca, G., Monaco, C., et al. (2020). Regional deformation and offshore crustal local faulting as combined processes to explain uplift through time constrained by investigating differentially uplifted Late Quaternary paleoshorelines: The foreland Hyblean Plateau, SE Sicily. *Tectonics*, 39, e2020TC006187. <https://doi.org/10.1029/2020TC006187>

Received 6 MAR 2020

Accepted 20 OCT 2020

Accepted article online 30 OCT 2020

Regional Deformation and Offshore Crustal Local Faulting as Combined Processes to Explain Uplift Through Time Constrained by Investigating Differentially Uplifted Late Quaternary Paleoshorelines: The Foreland Hyblean Plateau, SE Sicily

M. Meschis¹ , G. Scicchitano² , G. P. Roberts¹ , J. Robertson¹ , G. Barreca^{3,4} , C. Monaco^{3,4,5} , C. Spampinato⁶ , D. Sahy⁷ , F. Antonioli⁸ , Z. K. Mildon⁹ , and G. Scardino² 

¹Department of Earth and Planetary Sciences, Birkbeck, University of London, London, UK, ²Dipartimento di Scienze della Terra e Geoambientali, Università degli Studi di Bari Aldo Moro, Bari, Italy, ³Dipartimento di Scienze Biologiche, Geologiche e Ambientali, University of Catania, Catania, Italy, ⁴CRUST-Centro interUniversitario per l'analisi SismoTettonica tridimensionale con applicazioni territoriali, Chieti, Italy, ⁵Istituto Nazionale di Geofisica e Vulcanologia (INGV-OE), Catania, Italy, ⁶Portable Lab Geology and Engineering s.r.l.—Academic Spinoff, University of Catania, Catania, Italy, ⁷British Geological Survey, Keyworth, UK, ⁸Istituto Nazionale di Geofisica e Vulcanologia, Rome, Italy, ⁹School of Geography, Earth and Environmental Sciences, University of Plymouth, Plymouth, UK

Abstract Quaternary uplift is well documented in SE Sicily, a region prone to damaging seismic events, such as the 1693 “Val di Noto” earthquake (M_w 7.4), the largest seismic event reported within the Italian Earthquake Catalogue, whose seismogenic source is still debated and, consequently, the long-term seismic hazard is poorly understood. However, the spatial variation in the timing and rates of uplift are still debated, so it is difficult to link the dominant tectonic process(es) responsible for the uplift and the location of seismogenic sources. To better constrain the uplift rate, we have refined the dating of Late Quaternary marine terraces, using a synchronous correlation approach, driven by both published and newly obtained numerical age controls ($^{234}\text{U}/^{230}\text{Th}$ dating on corals). This has allowed recalculation of uplift rates along a N-S oriented transect within the Hyblean Plateau (HP) foreland region. Consequently, we have mapped the geometry of paleoshorelines along a coastline-parallel transect and hence the rates of uplift. The results suggest increasing uplift rate from south to north across the HP and that uplift rates have remained constant through the Late Quaternary. This spatially changing but temporally constant uplift places constraints on the proportion of uplift produced by regional geodynamic processes versus produced by local faults, such as an offshore east dipping active normal fault. We discuss these new findings in terms of the long-term seismic hazard for one of the most seismically active regions in the Mediterranean Basin.

1. Introduction

The complexity of deformation in regions subject to a combination of collision, subduction, mantle flow, regional uplift, extension, and volcanism leads to uncertainty in seismic hazard assessment and quantification of geodynamic processes. For example, the Hyblean Plateau (HP), SE Sicily in southern Italy, lies in a zone of active convergence, south of Etna volcano and close to offshore active normal faults. Quaternary uplift and active faulting in the HP is evidenced by a well-exposed sequence of raised marine terraces (Bianca et al., 1999; Monaco & Tortorici, 2000), and the occurrence of large earthquakes such as the 1693 “Val di Noto” earthquake (M_w 7.4) (Guidoboni et al., 2007). However, the mechanism(s) producing these uplifted terraces, and the links between uplift, regional tectonics and local active faulting are still highly debated. In particular, previous studies have suggested that the uplift in the HP is (i) produced by the long-term of the faulting activity of a normal fault, so-called the Western Fault (Bianca et al., 1999) and (ii) interpreted as a positive flexural bulge at the front of the Sicilian chain produced by the orogenic load

and the slab pull of the subducting Ionian slab (Billi et al., 2006; Cogan et al., 1989; Pedley & Grasso, 1992). This controversy needs to be addressed and new and refined crustal deformation rates can be the base for future works, investigating the region that hosted the earthquake with highest estimated magnitude (1693 Val di Noto earthquake— M 7.4) within the Italian earthquake catalog (Guidoboni et al., 2007).

This paper uses observations of the uplifted marine terraces to refine the chronology and spatial extent of the uplift. In particular, we map the inner edges of marine terraces, provide new estimated and refined ages for undated marine terraces and hence inner edges. This is done by applying a methodological approach so-called synchronous correlation technique, (i) driven by previous submerged paleoshorelines knowledge (Dutton et al., 2009) and (ii) supported by new $^{234}\text{U}/^{230}\text{Th}$ dating. Overall, this produces a correlation between inner edge ages and ages of global glacio-eustatic sea level highstands, useful to determine uplift rate scenarios that explain the observations. The results are used to discuss the relative influences of the doming effect from Mt. Etna located north of the HP (De Guidi et al., 2014), active normal faulting located offshore to the east (Argnani et al., 2012; Argnani & Bonazzi, 2005; Bianca et al., 1999; Monaco & Tortorici, 2000) and regional Africa-Eurasia collision/subduction processes including regional uplift associated with mantle flow (Barreca et al., 2016; Grad & Tiira, 2009; Neri et al., 2002; Westaway, 1993). We suggest that the ongoing uplift affecting the HP is related to a combined effect of prominent mantle flow/crustal thickening processes (e.g., Ferranti et al., 2006) and a less striking long-term footwall uplift from the offshore western normal fault.

2. Geological Background

The tectonic setting of SE Sicily is dominated by the ~N-S Neogene to Quaternary tectonic convergence between the European and African continental margins (Dewey et al., 1989; Faccenna et al., 2001). Progressive tectonic convergence has led to the formation of the Sicilian-Maghrebian chain and the Apennines, connected by the arc-shaped Calabrian Arc (Figure 1), which represents the subaerial portion of a larger accretionary prism in the Ionian Sea. It is the result of the Pliocene-Quaternary subduction of the Ionian realm, a 15–20 km thick crustal remnant (Catalano et al., 2001) of the Permo-Triassic “Neo-Tethys” ocean (Sengör, 1979). To the west, it is adjacent to the Pelagian Block (Ben-Avraham & Grasso, 1991; Nicolich et al., 2000; Torelli et al., 1998), which also includes the 25–30 km thick continental crustal portion of the HP in SE Sicily (Dellong et al., 2018, 2020). The transition from continental to oceanic material occurs along the Malta Escarpment in the near offshore of SE Sicily (Figure 1a), a Mesozoic passive margin which has been reactivated by oblique extension during the Quaternary (Bianca et al., 1999; Hirn et al., 1997).

The HP represents the onshore portion of a larger foreland domain, belonging to the Pelagian Block (Ben-Avraham & Grasso, 1991; Burolet et al., 1978; Cultrera et al., 2015; Grasso & Lentini, 1982). In particular, the HP, within the Hyblean-Malta Platform in the central Mediterranean, represents a carbonate promontory of the larger African paleomargin (Grasso & Lentini, 1982). Geological and seismic studies have shown a 6 km-thick Meso-Cenozoic sedimentary carbonate succession with intercalated volcanic layers, which overlie the Paleozoic basement; in places this carbonate succession has been overlain by Quaternary marine deposits associated with sequences of paleoshorelines (Bianca et al., 1999; Lentini et al., 1987).

Neogene tectonic shortening has affected the northern margin of the Pelagian Block producing a NE-SW oriented SE-verging thrust and fold system to the northwest (the Sicilian Chain) and normal faulting on the HP (Cultrera et al., 2015; Grasso et al., 1995). Convergence to the northwest is currently accommodated by a regional-scale, northward deepening crustal seismogenic structure (named the Sicilian Basal Thrust SBT; Figure 1b) whose focal mechanisms are compatible with a nearly N-S shortening and with some field evidence of active folding and thrust deformation at the Sicilian chain front (Lavecchia et al., 2007). In particular, in the NW sector of Mt. Etna volcano the earthquakes reach a maximum depth of about 35 km (De Guidi et al., 2015; Lavecchia et al., 2007). Indeed, the northern rim of the HP, where the Scordia-Lentini Graben (SLG) is mapped (Figure 1a), is thought to be seismically active, yet it only partially accommodates (~50% of the total 10 mm/yr of convergence rate) the ongoing Africa-Eurasia convergence measured with the GPS system along a N-S oriented transect in SE Sicily (Chiarabba & Palano, 2017; DeMets et al., 2015; Ferranti et al., 2008; Mastrolembo Ventura et al., 2014; Mattia et al., 2012; Musumeci et al., 2014; Palano et al., 2012). This is also consistent, for instance, with the process of tectonic inversion

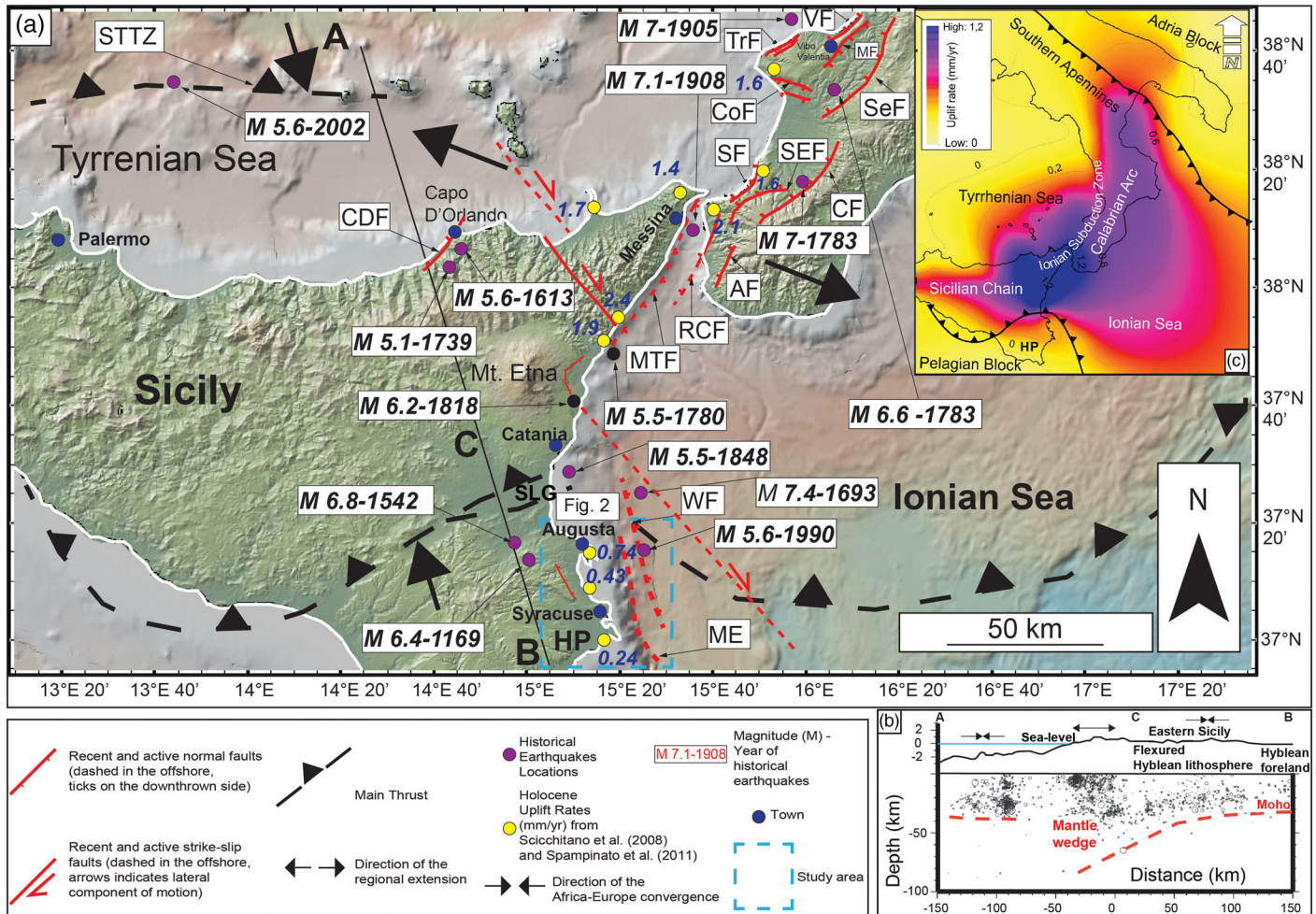


Figure 1. (a, b, and c) Tectonic maps and cross section showing Late Quaternary to present deformation for Sicily and Calabria. The light blue-colored dashed square shows the investigated area lying in the HP. Black and purple dots show the location of historical earthquakes; yellow dots show values of Holocene uplift rates from Antonioli et al. (2006). In (b) a sketched cross section shows the seismicity distribution and the Moho discontinuity along the transect A-B adapted from Chiarabba and Palano (2017). In (c) rates of uplift mapped within the Calabrian Arc domain are shown from Ferranti et al. (2006). VF: Vibo Fault; TrF: Tropea Fault; MF: Mileto Fault; SeF: Serre Fault; CoF: Coccorino Fault; SEF: Sant'Eufemia Fault; SF: Scilla Fault; CF: Cittanova Fault; AF: Armo Fault; RCF: Reggio Calabria Fault; MTF: Messina-Taormina Fault; CDF: Capo D'Orlando Fault; WF: Western Fault; STTZ: Southern Tyrrhenian Thrust Zone; SLG: Scordia-Lentini Graben; ME: Malta Escarpment.

mapped north of Augusta town within the SLG where extensional faults have been reactivated as high-angle thrust faults since 0.85 Ma (Mastrolembo Ventura et al., 2014; Mattia et al., 2012; Tortorici et al., 2006). For some, the seismogenic source of the 9 January 1693 earthquake (M_w 6), interpreted as a foreshock of the 11 January 1693 earthquake (M_w 7.4), could be located within the tectonically inverted graben north of Augusta (Mastrolembo Ventura et al., 2014).

The tectonic evolution over the Quaternary of eastern Sicily has also involved crustal extension accommodated by normal faults. These include (i) the offshore Messina-Taormina Fault in the north, which produced the most damaging earthquakes recorded in Europe in the 20th and 21st centuries, such as the 1908 Messina earthquake (M 7.1) (e.g., Aloisi et al., 2013; Meschis et al., 2019, for review), and (ii) an east dipping normal fault system located mostly offshore in the south (Argnani et al., 2012; Argnani & Bonazzi, 2005; Bianca et al., 1999); the HP lies in the footwall of this east dipping normal fault system. Evidence for present-day activity on this east dipping fault system includes basins infilled by synrift clastic wedges and marine Quaternary deposits that thicken toward the boundary faults (Argnani & Bonazzi, 2005; Bianca et al., 1999). For instance, one of the offshore faults, named the Western Fault, has been claimed to be the seismogenic source of the 1693 seismic event (see also Azzaro & Barbano, 2000; Jacques et al., 2001; Piatanesi &

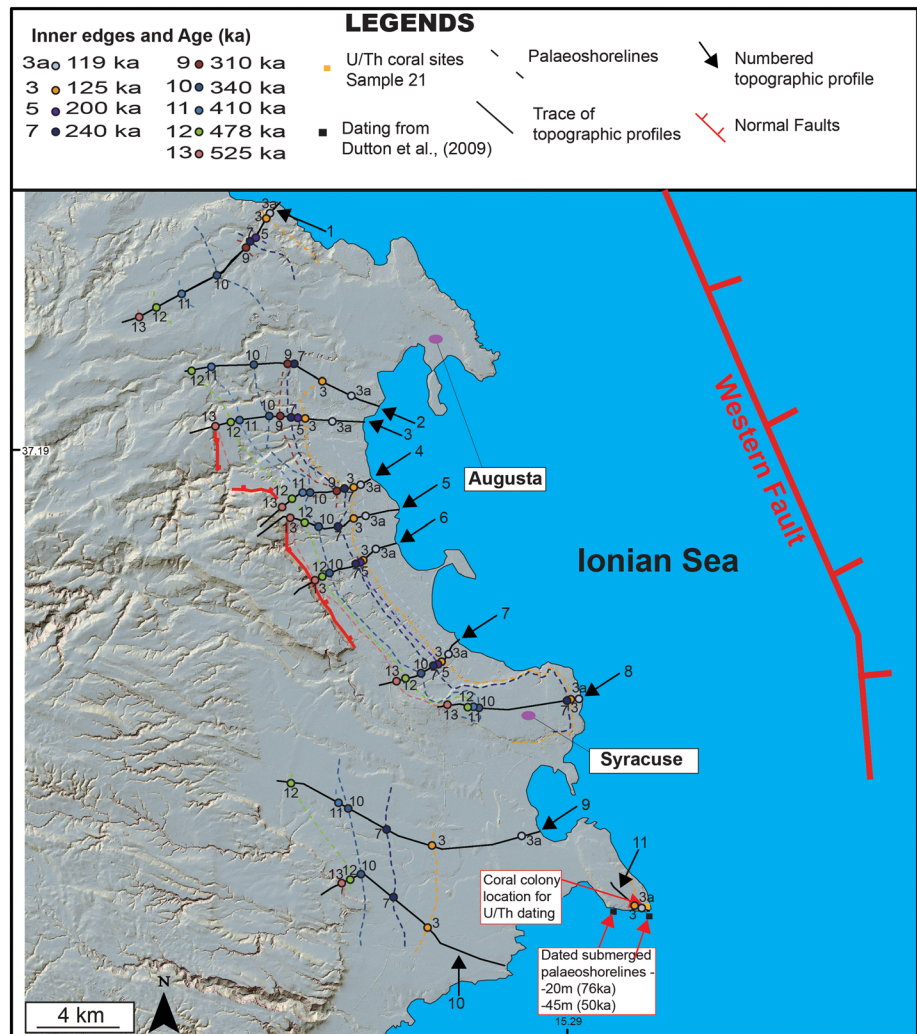


Figure 2. Location maps for paleoshorelines within the HP, SE Sicily. A 2 m resolution DEM with the associated shaded relief to highlight breaks of slope is used as base map. Dashed colored lines represent the inner edge of successive mapped paleoshorelines. Locations where corals for U/Th dating have been collected and where available age controls from dated submerged paleoshorelines used in this paper are shown. Numbered black lines indicate the 12 topographic profiles within the investigated area. Numbered dots represent inner edges location for paleoshorelines, detailed in Table 4. Note that only 30 out of 50 km are shown for the offshore Western Fault (solid red line). The entire fault length is shown in Figure 1.

Tinti, 1998, among others), which is the highest magnitude earthquake reported within the official Italian Catalogue of Earthquakes (Guidoboni et al., 2007). Alternative suggested seismogenic sources for the 1693 “Val di Noto” earthquake have been associated to (i) a segment of the south verging, north dipping Sicilian Basal Thrust at the front of the Apennine-Maghrebian chain (Lavecchia et al., 2007), (ii) two opposite-verging compressional faults at the front of the chain (INGV-DISS Working Group, 2018) and (iii) a portion the Ionian subduction plane (Gutscher et al., 2006).

Quaternary processes related to the interaction between sea level changes, regional uplift, and crustal deformation have produced sequences of marine terraces mostly outcropping on the eastern part of the HP (Bianca et al., 1999; Monaco et al., 2002). Despite the paucity of numerically dated paleoshorelines and marine terrace deposits, previous geoscientists have attempted to investigate the uplift process affecting the HP by applying a “sequential” correlation approach, obtaining uplift rates of 0.65 mm/yr (Bianca et al., 1999). However, the “sequential” correlation approach may fail where age control is lacking, and low uplift rates may have allowed erosion of some paleoshorelines. For instance, for the offshore Western Fault slip rates

>3 mm/yr over the Late Quaternary have been suggested using the interpreted age of terraces carved within the onshore footwall in SE Sicily as age constraints (Bianca et al., 1999). However, these age estimates for paleoshorelines may be affected by the overprinting problem (Meschis et al., 2018; Pedoja et al., 2018; Roberts et al., 2009, 2013; Robertson et al., 2019), and further study and robust dating is required. Furthermore, the uplift was only attributed to the footwall uplift of the offshore Western Fault (Bianca et al., 1999).

In particular, a prominent sequence of uplifted Late Quaternary paleoshorelines, is located between the Augusta peninsula in the north of the HP, to south of Syracuse town (Bianca et al., 1999). The ages of these paleoshorelines have been poorly constrained, due to the lack of absolute age controls in the region, so uplift rates over the Late Quaternary have been uncertain. Furthermore, the “overprinting problem” occurs because Late Quaternary sea level highstands are not all exactly at the elevation of present sea level, and those lower than present sea level may have their paleoshorelines destroyed by younger, higher sea levels, if uplift is not great enough to raise them above the wave erosion zone. Thus, simply assigning the next highest paleoshoreline to the next oldest sea level highstand age is prone to fail if some paleoshorelines are not preserved (Meschis et al., 2018; Pedoja et al., 2018; Roberts et al., 2009, 2013; Robertson et al., 2019), and this may be why the temporal and spatial pattern of uplift is still debated. Regardless of whether the uplift is related to the offshore crustal extension, regional processes, a combination of these, or the doming effect from Mt. Etna, previous studies show evidence of differential uplift within the HP (Antonioli et al., 2006; Bianca et al., 1999; Ferranti et al., 2006; Spampinato et al., 2011). However, it is still unclear if this uplift and the associated rates have been constant or fluctuating over the Late Quaternary, suggesting that more investigations are needed for an improved long-term seismic hazard assessment.

Furthermore, we highlight the existence of an underutilized source of uplift rate information. Constraints on the uplift rate can be gained by study of the ages of submerged paleoshorelines offshore Syracuse town (Dutton et al., 2009) (Figure 2 for locations). Two submerged paleoshorelines have been mapped at -20 and -45 m under the present-day sea level. The ages of these paleoshorelines have been constrained using $^{234}\text{U}/^{230}\text{Th}$ dating of calcite speleothems that grew subaerially during sea level lowstands, and ^{14}C dating of layers of calcitic serpulids that encrusted the speleothems when the caves and speleothems were later flooded. These age constraints show that the shallower paleoshoreline formed before 74 ka (Dutton et al., 2009). The deeper one at -45 m formed before 44 ka. In this paper, we will test whether using the above mentioned numerical ages, allows these submerged paleoshorelines to be assigned to the Marine Isotope Stage (MIS) 5.1 sea level highstand (76/80 ka, -20 m) and the MIS 3.3 sea level highstand (50 ka, -45 m).

2.1. Characteristics of the Mapped Uplift

This paper focusses on observations of uplift so an important starting point is to note that uplift varies on both long and short wavelengths within Southern Italy.

For example, evidence exists for long-wavelength uplift (Figure 1c), probably produced by mantle flow around the edges of the subducting slab at depth (Lucente et al., 2006), evidenced by observations of seismic tomography and seismic anisotropy. Significant regional uplift affects Calabria and NE Sicily, which progressively vanishes toward Apulia region to the north and HP to the south (Faccenna et al., 2011; Ferranti et al., 2006; Westaway, 1993). This large-scale topographic bulge, recorded by uplift and deformation of the MIS 5e terrace (125 ka) (Figure 1c; Ferranti et al., 2006), is suggested to originate from subcrustal mantle flow and spans a wider lithospheric area than the subducted Ionian slab underneath the southern Tyrrhenian Sea, which is traditionally claimed as the source for Calabria “regional” uplift (Faccenna et al., 2011; Gvirtzman & Nur, 2001; Westaway, 1993). As a consequence, it reaches a maximum rate above the Ionian subduction zone in southern and central Calabria with uplift rates >1 mm/yr especially where the Ionian slab is detached (Barreca et al., 2016; Faccenna et al., 2011; Roberts et al., 2013; Scarfi et al., 2018), while lower uplift rates (decreasing to 0) are recorded in the Taranto Gulf and SE Sicily coast within the HP (Dutton et al., 2009; Ferranti et al., 2006).

On a shorter wavelength, uplift variations have been noted along the strike of active normal faults in Calabria and Sicily and others areas associated with subduction, due to displacement gradients along the faults (e.g., Ferranti et al., 2007; Giunta et al., 2012; Meschis et al., 2018; Roberts et al., 2013). For

example, extension between the Ionian domain and the Hyblean-Malta block affects the region offshore the HP (Palano et al., 2012), where active extension is accommodated by east dipping normal faults producing seismic events like the 1990 “Santa Lucia” earthquake (M_w 5.6) (Argnani & Bonazzi, 2005; Bianca et al., 1999; Monaco & Tortorici, 2000). Of particular importance here is the existence of a ~50 km-long, east dipping normal fault, named Western Fault, mapped ~14–20 km offshore the investigated area, deforming Quaternary deposits and in places producing a fault scarp on the seafloor (Argnani et al., 2012; Argnani & Bonazzi, 2005). Some have hypothesized that this offshore fault may produce uplift within the HP (Bianca et al., 1999).

Thus, the combination of both long and short wavelength processes emphasizes the need for robust constraints on the spatial and temporal variations in uplift across the HP if the relative contributions of different processes responsible for the uplift are to be ascertained.

3. Approach and Methods

In this section, we present how we approach our attempts to constrain and refine spatial and temporal variations in uplift across the HP, in order to find if this uplift is driven by one or multiple mechanisms. We describe the method for each step in the study in turn below.

3.1. DEM-Based Topographic Analysis and Field Mapping of Uplifted Late Quaternary Paleoshorelines

We have undertaken detailed geographic information system (GIS)-based geomorphological analysis, by using 2 m high resolution digital elevation model (DEM) kindly provided by “Regione Siciliana” (Sicilian Region office), alongside field mapping of paleoshorelines (Figure 2). Our DEM-based topographic analysis used the approach from previous studies of uplifted paleoshorelines in the Mediterranean Basin (e.g., Meschis et al., 2018; Roberts et al., 2013; Robertson et al., 2019). We conducted new mapping of sites where previously mapped paleoshorelines had been identified (Bianca et al., 1999), and in many locations confirmed the existence of prominent breaks of slope defining paleoshoreline inner edges, both in the field and on the DEM, mapping these breaks of slope along strike wherever possible. Paleoshoreline locations are predominantly paleorocky shorelines, characterized by (i) flat surfaces cut into bedrock by wave erosion, accompanied in places by shallow marine deposits lithified by early marine diagenesis (Meschis et al., 2018; Roberts et al., 2009, 2013; Robertson et al., 2019), (ii) caves, lithophagid borings, and notches at the updip terminations of wave-cut platforms (Ferranti et al., 2006; Firth & Stewart, 1996; Meschis et al., 2018; Roberts et al., 2013; Robertson et al., 2019), and (iii) millholes (or marine erosion pans) which are quasi-circular depressions developed on the wave-cut platform formed by the scouring action of pebbles as a result of wave action (Miller & Mason, 1994; Jennifer Robertson et al., 2019) (Figure 3). The combination of these three sets of features allowed us to interpret gently sloping seaward surfaces as paleoshoreface surfaces cut by wave action and bounded updip by paleo sea cliffs or rocky paleoshorelines, following the lead of previous marine terrace investigations (Armijo et al., 1996; Bianca et al., 1999; Gallen et al., 2014; Meschis et al., 2018; Roberts et al., 2009, 2013) (Figure 3). We used a handheld GPS with a built-in barometric altimeter to constrain paleoshoreline locations in terms of x , y , and z coordinates. Once mapped along strike in GIS, we constructed 12 topographic profiles across the DEM to help visualize the geometry of the deformed paleoshorelines and marine terrace deposits, marking locations on the profiles where paleoshorelines were identified in the field (Figure 2).

Field mapping was crucial because some marine terraces and paleoshorelines were clear on the DEM and in the field, but others were less clear to map on the DEM because detailed geomorphological fieldwork showed that (i) breaks of slope identified as paleo sea cliffs were rather small in height above the sloping terraced surface (less or equal to few meters) and (ii) the geographic extent of the terrace surfaces and wave-cut platforms were limited (a few meters across) and too small to resolve on DEMs (Figure 3). In general, the combined approach of mapping of paleoshoreline elevations from DEMs analysis and fieldwork allows a regional extensive coverage. Following the approach of previous studies (Meschis et al., 2018; Roberts et al., 2013; Robertson et al., 2019), regression analysis was applied to assess our mapping and correlations.



Figure 3. (a and b) Field photos showing the geomorphology of two successive paleoshorelines with mapped inner edges along Profile 8, shown in Figure 2. (c, d, and e) Field evidences are presented for a paleoshoreline, showing a scarp-like paleocliff with the presence of lithophagid borings and an associated limestone-made wave-cut platform with presence of millholes confirming wave action.

3.2. New $^{234}\text{U}/^{230}\text{Th}$ Dating of Corals

The fieldwork has involved sampling corals from marine terrace deposits for $^{234}\text{U}/^{230}\text{Th}$ dating (Figure 4). We identified a coral colony (*Cladocora caespitosa*) from a wave-cut platform at 14 m above sea level, south of Syracuse and landward of the two dated submerged paleoshorelines described by Dutton et al. (2009). Based on the position of the corals, we estimate that the colony formed on a substrate of lithified subwave base Quaternary bioclastic sands (calcarenite), and was bound by early marine cements, possibly at rising sea level highstand/stillstand. Lithophagids bored during wave erosion at highstand when the wave-cut platform formed (Figure 4). $^{234}\text{U}/^{230}\text{Th}$ dating was carried out at the Geochronology and Tracers Facility of the British Geological Survey, Keyworth, UK, using total dissolution methods outlined by Crémière et al. (2016), with isotope ratios measured on a Neptune Plus multicollector inductively coupled plasma mass spectrometer (MC-ICP-MS). Preparation of coral samples was a crucial step before $^{234}\text{U}/^{230}\text{Th}$ analysis. Millimeter-scale corallite fragments were isolated from carefully selected and systematically cleaned

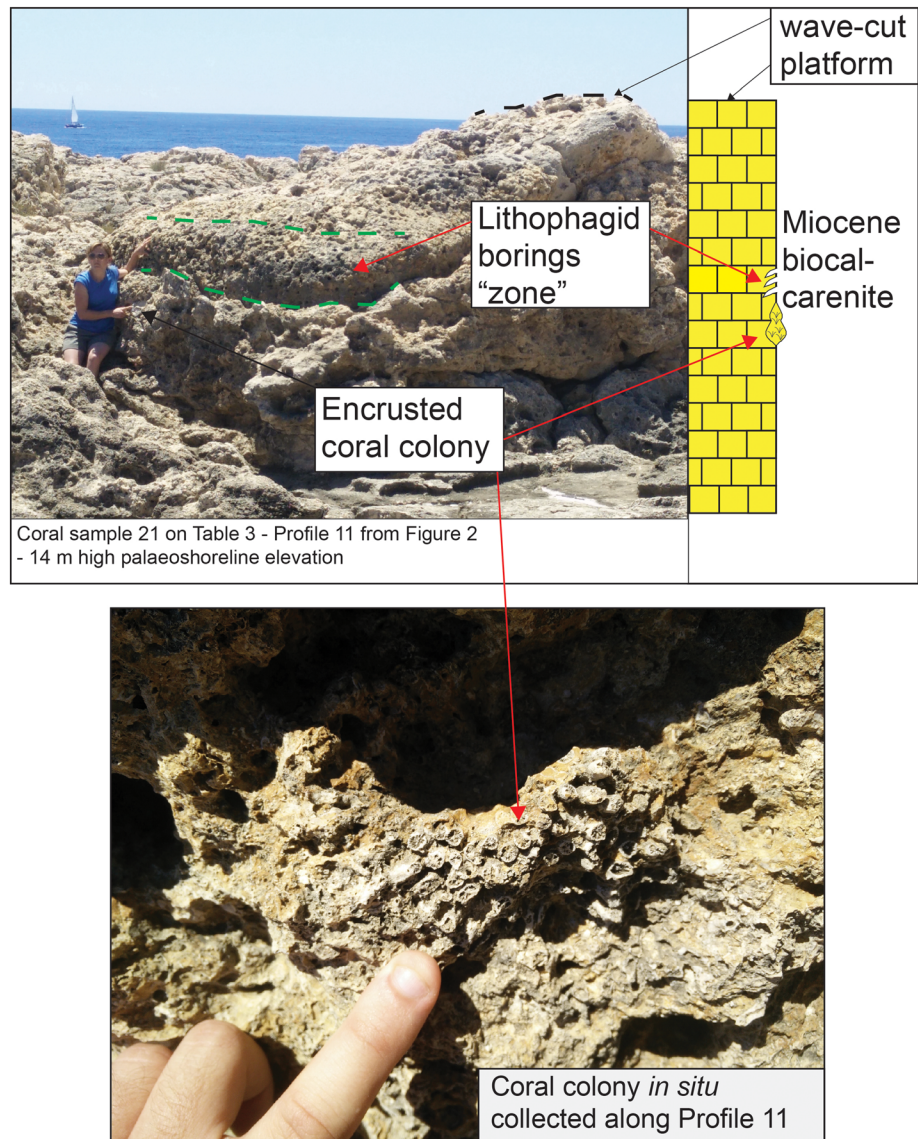


Figure 4. Field photos showing the sample location for a dated coral colony. The top photo shows an overview of where the coral colony was sampled for U/Th age determination, with a sketch stratigraphic log. Bottom photo shows details of the coral colony in situ.

sediment hand samples. Any material showing evidence of alteration and/or detrital matrix on the outside of the corallite wall was removed mechanically using a scalpel under a microscope and/or chemically by washing the wall with HCl (10%) for 5–10 s, followed by thorough rinsing with ultrapure water. Furthermore, coral septa were separated from the wall because they are thinner and more prone to diagenetic alteration processes (Roberts et al., 2009); only corallite walls were used for analysis in this paper. We also analyzed both bulk corallite fragments (2–10 mg) and powder subsamples obtained using a computer-controlled drill equipped with a 200 μm drill bit in order to avoid any portion of the coral that showed discolouration or other evidence of alteration.

3.3. Synchronous Correlation Approach to Assign Ages to Undated Paleoshorelines

In this paper, the synchronous correlation technique is adopted. This is based on the idea that sea level highstands, producing marine terraces in uplifting regions (Lajoie, 1986), are not equally spaced in time implying that the resultant marine terraces will not be equally spaced in elevation for any given uplift rate scenario

Table 1
Values of Sea Level Highstands Derived From Siddall et al. (2003) and Rohling et al. (2014) Used to Calculate Predicted Paleoshoreline Elevations Given a Value for Uplift Rate

Age (ka)	Elevation of highstands (mm)
0	0
30	-80,000
50	-60,000
76.5/80	-30,000
100	-25,000
115	-21,000
119	-5,000
125	5,000
175	-30,000
200	-5,000
217	-30,000
240	-5,000
285	-30,000
310	-22,000
340	5,000
410	-5,000
478	0
525	20,000
550	10,000
560	3,000
590	20,000
620	20,000
695	10,000
740	5,000
800	20,000
855	20,000
980	25,000

(Meschis et al., 2018; Roberts et al., 2013; Robertson et al., 2019; Westaway, 1993). For example, if the uplift rate is constant, relative vertical distances between paleoshorelines will be in phase with the relative time differences between glacio-eustatic sea level highstands but scaled differently, so simple iteration of the uplift rate can be used to recover the uplift rate that explains the observations through a best fit approach. However, note that this approach also works if the uplift rate changes through time, because uplift rate changes can also be incorporated into the iteration (e.g., Roberts et al., 2009, for an example of this). Note that for both constant and changing uplift rate scenarios, some paleoshorelines may be overprinted and hence not preserved on an uplifting coastline. This occurs where paleo sea level at a highstand was beneath the level of present-day sea level due to a smaller global ocean volume at that time, combined with a low uplift rate; these two factors combine so that a younger highstand with larger global ocean volume and higher paleo sea level elevation overtops and erodes the older paleoshoreline during sea level rise. Note that the synchronous correlation approach deals with this problem as all paleoshoreline elevations are calculated and displayed on profiles, whereas sequential correlation is prone to fail in this scenario if the problem is not identified (e.g., see Roberts et al., 2009, for further explanation). Also, it is desirable to have at least one paleoshoreline with age control in order to assume, as first step, a constant uplift rate through time and assess whether the iteratively calculated sea level highstand elevations match the elevations of measured and mapped paleoshorelines. If they do not, then a different scenario involving changing uplift rate through time is investigated, iterating uplift rates driven by age controls, in order to find the best match with measured paleoshoreline elevations. This approach was described in detail in Houghton et al. (2003), Roberts et al. (2009, 2013), Meschis et al. (2018), and Robertson et al. (2019).

Note that we have used sea level curves from Siddall et al. (2003) and Rohling et al. (2014) for our synchronous correlation approach (Table 1). However, some can argue that using different sea level curves can lead to obtain different final results for derived uplift rates. Yet, Robertson et al. (2019) shows that the use of other sea level curves (e.g., Waelbroeck et al., 2002) makes a minimum difference to retrieve rates of uplift.

To perform the synchronous correlation, topographic profiles are made intercepting the paleoshorelines from DEM data (Figure 2). Then, using data from fieldwork to corroborate the topographic profile, interpretations are undertaken of the inner-edge elevations of paleoshorelines (e.g., Meschis et al., 2018; Roberts et al., 2013; Robertson et al., 2019). Paleoshoreline elevations from GIS analysis corroborated in the field are then input into a spreadsheet called the “Terrace Calculator” (Roberts et al., 2009, 2013). We start our modeling with an initial uplift rate scenario, constant through time, for each topographic profile, constrained by using one or more age controls for dated paleoshorelines. This has allowed us the iteration of uplift rates in order to calculate the expected sea level highstands elevations for undated paleoshorelines and compare them to those measured on DEM and in the field. Linear regression analysis, calculating the coefficient of determination R^2 , quantifies the relationship between the predicted and measured paleoshoreline elevations. In this paper, we iterate uplift rates, driven by age controls, aimed to find the best match between all mapped or “measured” uplifted paleoshoreline elevations on a topographic profile and the “predicted” elevations which represent the sea level highstands from well-accepted and known sea level curves in the Late Quaternary (Rohling et al., 2014; Siddall et al., 2003) (Table 1), forcing the user to maximize the coefficient of determination (R^2 value) for a linear regression analysis through all paleoshoreline elevation data. Error bars on this linear regression analysis are assigned considering that DEMs used from “Regione Siciliana” have a 2 m resolution, and the “predicted” elevations iteratively calculated using well-known sea level curves (Rohling et al., 2014; Siddall et al., 2003) have 12 m of error on each sea level highstand. Furthermore, root-mean-square (RMS) deviation calculations were conducted in order to identify the best fit and then the best uplift rate value. In particular, following an approach from previous studies (Meschis

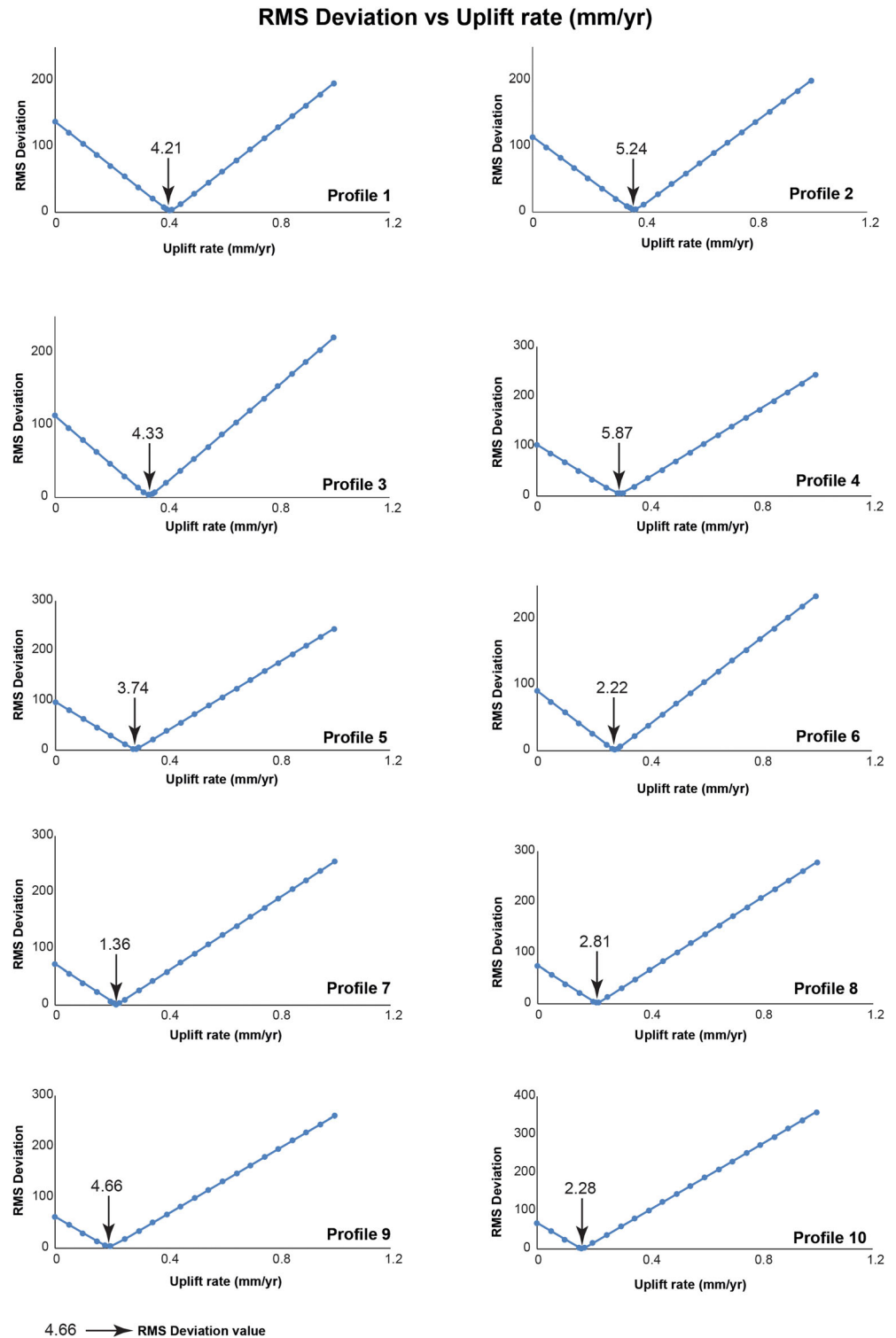


Figure 5. Results of synchronous correlation investigation of uplift rates. Root-mean-square deviation values are calculated for each topographic profile for all uplift scenarios from 0 to 1 mm/yr at intervals of 0.05 mm/yr in order to show the best fit between “measured” and “predicted” paleoshorelines elevations. The RMS values illustrate the misfit between measured and predicted paleoshoreline elevations during iteration of the uplift rate. The uplift rate with the lowest RMS misfit is preferred (refer to Figures 6 and 7 for visualization of individual profiles).

Topographic Profile 11 with modelled shoreline elevations

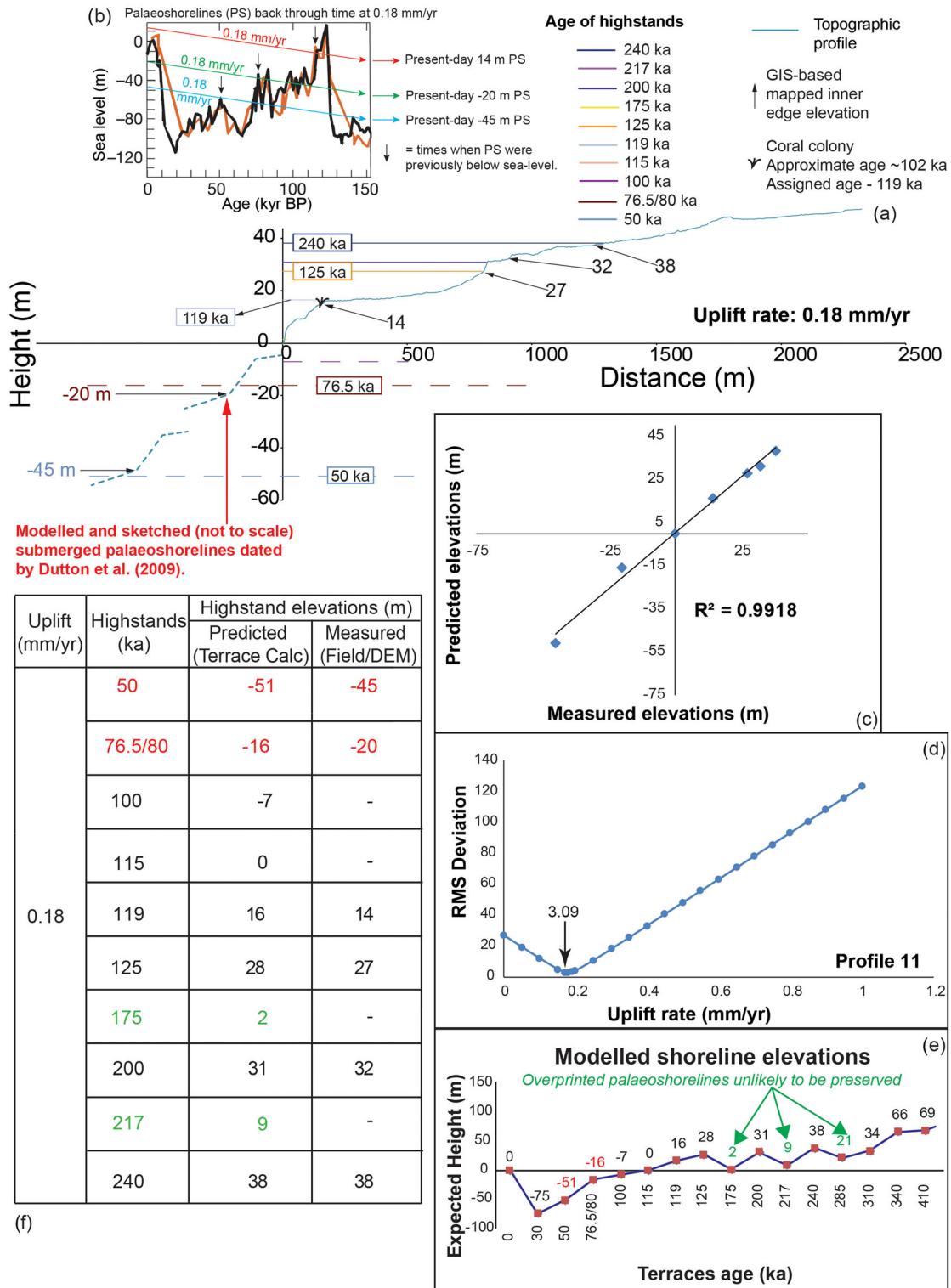


Figure 6. (a) Topographic Profile 11 (see profile location in Figure 2) showing paleoshoreline elevations predicted by synchronous correlation. (b) Paleoshoreline elevations through time relative to the sea level curves of Siddall et al. (2003). (c, d, and e) A synchronous correlation approach is applied driven by ages assigned to the submerged paleoshorelines in order to find the best match between “measured” and “predicted” elevations. Note that some sea level highstands like 175 and 217 ka are lower than the next younger highstand, suggesting they may well be overprinted, that is, removed by erosion during rising sea level during the subsequent highstand. (f) Table showing derived values.

et al., 2018; Robertson et al., 2019), for each topographic profile precise values of uplift rates were gained by iterating values of uplift rates from 0 to 1 mm/yr at intervals of 0.05 mm/yr and plotting the RMS deviation values gained, from comparing the values of the measured/mapped versus predicted paleoshoreline elevations (Figure 5).

3.4. Vertical Deformation Modeling to Estimate the “Footwall Uplift” Effect of the Western Fault

To investigate the possible influence of offshore normal faulting, and the role of possible footwall uplift of the Western Fault, we conducted elastic half-space modeling using *Coulomb 3.4* (Toda et al., 2011). We use the published trace of the fault which reveals changes in strike along the fault length (Argnani et al., 2012). The fault trace is incorporated into the modeling using the method and Coulomb software plug-in from Mildon et al. (2016), that uses the nonlinear fault trace, with along-strike bends, to produce a corrugated 3-D fault surface. There is debate about the dip of the fault (Argnani et al., 2012; Bianca et al., 1999) and so we varied the modeled dip value between 30° (e.g., Argnani et al., 2012) and 70° (e.g., Bianca et al., 1999). We used a concentric slip distribution consistent with scaling relationships between fault length, earthquake magnitude and slip at depth and at the surface (Wells & Coppersmith, 1994), in order to obtain an earthquake magnitude $\sim M_w$ 7 (we used a value of M_w 7.05). The implied uplift contours were then converted into uplift rate values over the Late Quaternary by assuming a value of 500 yr for earthquake recurrence as suggested previously by some (Bianca et al., 1999) on the offshore Western Fault, as the historical record implies that $\sim M_w$ 7 events are unlikely to recur at $< \sim 500$ yr intervals. Finally, we extracted the uplift rate field along the modern-day coastline to calculate the effect of footwall uplift on the mapped paleoshorelines.

4. Results

Our mapping identified up to 12 paleoshorelines, and some of these could be mapped along strike for many kilometers (Figures 2–9). However, note that in some areas we were unable to link paleoshorelines along strike. Nonetheless, we suggest the paleoshoreline locations and continuity along strike we derived are similar to those published by others, confirming their mapping (e.g., Bianca et al., 1999), and adequate for our purposes. However, we conducted synchronous correlation to check and refine the ages for paleoshorelines suggested by Dutton et al. (2009) and Bianca et al. (1999).

Figure 6a shows our attempt to correlate sea level highstands to submerged paleoshorelines mapped by Dutton et al. (2009). In particular, these authors analyzed a speleothem sampled in a cave carved within a submerged paleocliff, identifying a sea level highstand, at -20 m and obtained an age of ~ 74 ka (Table 2) with a growth rate of ~ 10 cm/kyr which, while relatively rapid, is not unprecedented in the speleothem literature (e.g., Gascoyne et al., 1983; Goede & Vogel, 1991; Mickler et al., 2006; Musgrove et al., 2001; Niggemann et al., 2003). We stress that growth rates for speleothems can vary over 3–4 times of magnitude, with a range of 0.001 and 1 mm/yr (100 cm/kyr) (Ford & Williams, 2007). These rates depend on several factors (local hydrology, soil/vegetation cover above the cave, airflow through the cave, etc.), suggesting that even within a single cave it is possible to have very different rates for different speleothems. It is important to note that some growth rates for speleothems from the Last Interglacial Maximum (LIM) in southern Turkey and northern Italy (Corchia Cave) have been estimated around 40 cm/kyr (Drysdale et al., 2009; Rowe et al., 2020). Therefore, it is plausible that speleothems taken into account for this study started rapidly growing subaerially immediately after the sea level fall during the transition between MIS 5a sea level highstand (80.0 ka) and the successive lowstand, which shows the most rapid sea level fall of the Late Quaternary (Cutler et al., 2003). This suggests that the submerged paleoshoreline at -20 m could belong to the MIS 5a (80.0 ka) sea level highstand and is here used as an age control (Table 2). It is important to note that the idea of assigning the -20 m submerged paleoshoreline to the MIS 5a (80 ka) is supported by the fact that there is no striking evidence for this paleoshoreline to be older, and it is unlikely due to the overprinting problem. This is a common problem, when one works with raised paleoshorelines in regions affected by relatively low uplift rates, recognized worldwide and in particular in the Mediterranean realm (e.g., Anderson et al., 1999; Caputo et al., 2010; Pedoja et al., 2018; Roberts et al., 2013; Robertson et al., 2019). For instance, Figure 6e shows that claiming an older age, as previously suggested of 175 ka (MIS 6d) (Dutton et al., 2009), is unlikely because of the overprinting problem. However, we cannot completely rule out the possibility that this submerged paleoshoreline has not undergone a prominent and/or total

Table 2
Age Controls Derived From Two Submerged Paleoshorelines Available in the Literature

Reference	Dating method	Dated sample description	Profile number	Assigned highstand (ka)	Paleoshoreline elevation (m a.s.l.)
Dutton et al. (2009)	U/Th	“Three specimens of stalagmite.”	11	76.5/80	−20
Dutton et al. (2009)	U/Th	“A specimen of stalactite.”	11	50	−45

Note. Locations are shown in Figure 2.

overprinting process, and thus it could be older, but more investigations would be needed. Likewise, a deeper cave carved within a submerged paleocliff identifying a sea level highstand mapped at −45 m could belong to the MIS 3c (50 ka), given that the dated speleothem shows an age of 44 ka, as previously suggested (Dutton et al., 2009) (Table 2).

Using these elevations/depths and age control, we iterated values for uplift rates, using an initial “constant rate through time” scenario to find the best match between mapped paleoshorelines, both offshore and onshore, and the predicted sea level highstand elevations. We find our preferred uplift rate of 0.18 mm/yr constant through time, a value in relatively close agreement with the 0.2 mm/yr suggested by Dutton et al. (2009) (Figure 6a). The robustness of our correlation is assessed by linear regression in Figure 6b where a coefficient of determination R^2 value >0.99 is found. Moreover, we calculate RMS deviation in order to find the best possible value of uplift rate as shown in Figure 6c, as proposed by previous studies (Meschis et al., 2018; Robertson et al., 2019). Figure 6d and the associated table show the sea level curve modeled using our preferred uplift rate, suggesting which sea level highstands and their predicted elevations will be preserved in the landscape. This is also supported by a new approximate age control from $^{230}\text{Th}/^{234}\text{U}$ dating on a coral sampled at 14 m in the same topographic profile (Profile 11) presented in Figure 6. Corals from this colony have proved to be difficult to date, as nine out of the 10 analyzed subsamples showed evidence of open system behavior, that is, U and/or Th exchange between the sample and its environment over time, to an extent that precludes age interpretation. The remaining sample gave an age of 102 ka, with an unusually low initial $\delta^{234}\text{U}$ value of 103.2‰ (Table 3) which appears to be consistent with precipitation from a mixture of seawater ($\delta^{234}\text{U} \sim 145\%$) and the freshwater similar to that from which the speleothems analyzed by Dutton et al. (2009) precipitated ($\delta^{234}\text{U} \sim 60\%$). Furthermore, Table 3 shows a low value of U content (1.4 ppm), if compared to more reliable studies where U content for corals are close to 3 ppm (Dutton, 2015), suggesting for this paper U loss possibly due to leaching of U by freshwater. Although the calculation of the age gives ± 1.7 kyr as error (Table 3), we think that the unusually low initial $\delta^{234}\text{U}$ value suggests that we should use this calculated age with caution. For instance, in the Gulf of Aqaba, raised paleoshorelines have been investigated and by applying U/Th dating corals have been dated; some of them have shown low values of $\delta^{234}\text{U}$, and the calculated coral ages could actually be older as suggested by El-Asmar (1997). This would suggest that our calculated coral age of 102 ka in this paper can be older and thus

Table 3
Measurements of U/Th Isotope Ratios of a Coral Sample Collected Near Syracuse Town

Sample	Weight (mg)	U (ppm)	Th (ppm)	$(^{230}\text{Th}/^{232}\text{Th})$	$(^{232}\text{Th}/^{238}\text{U})$	$(^{230}\text{Th}/^{238}\text{U})$	$(^{234}\text{U}/^{238}\text{U})$	Age (ka)	$\delta^{234}\text{U}_i$	Assigned age (ka)
18	3.18	1.09	0.108	40.0	0.03246 ± 0.00004	1.299 ± 0.004	1.096 ± 0.003	—	—	—
19	4.03	1.11	0.181	22.7	0.05372 ± 0.00005	1.221 ± 0.004	1.097 ± 0.002	—	—	—
20A	3.96	0.94	0.167	22.5	0.05861 ± 0.00007	1.320 ± 0.004	1.104 ± 0.003	—	—	—
20B	0.46	0.85	0.027	142.4	0.01042 ± 0.00002	1.484 ± 0.013	1.107 ± 0.008	—	—	—
20C	0.19	0.68	0.107	34.2	0.05185 ± 0.00039	1.774 ± 0.027	1.136 ± 0.016	—	—	—
20D	0.25	0.29	0.159	16.2	0.17930 ± 0.00257	2.908 ± 0.067	1.023 ± 0.027	—	—	—
21A	10.0	0.93	0.324	11.2	0.11412 ± 0.00007	1.281 ± 0.003	1.102 ± 0.002	—	—	—
21B	1.24	0.73	0.033	117.2	0.01458 ± 0.00002	1.709 ± 0.013	1.109 ± 0.006	—	—	—
21C	0.67	1.40	0.020	142.6	0.00465 ± 0.00001	0.662 ± 0.005	1.108 ± 0.006	102.0 ± 1.7	103 ± 8	119 (?)
21D	0.54	0.64	0.053	61.1	0.02754 ± 0.00007	1.684 ± 0.020	1.134 ± 0.009	—	—	—

Note. The location of the collected corals is shown in Figure 2. Activity ratios were corrected for instrumental effects (mass bias, secondary electron multiplier vs. Faraday cup yield, and hydride formation and tailing) and the contribution of naturally occurring U and Th isotopes from the ^{229}Th - ^{236}U isotopic tracer and were calculated using the decay constants of Cheng et al. (2013). Age and initial $\delta^{234}\text{U}$ were calculated assuming an initial detrital ($^{232}\text{Th}/^{238}\text{U}$) of 1.2 ± 0.6 with secular equilibrium in the ^{238}U decay chain. All uncertainties are quoted at the 2 sigma level.

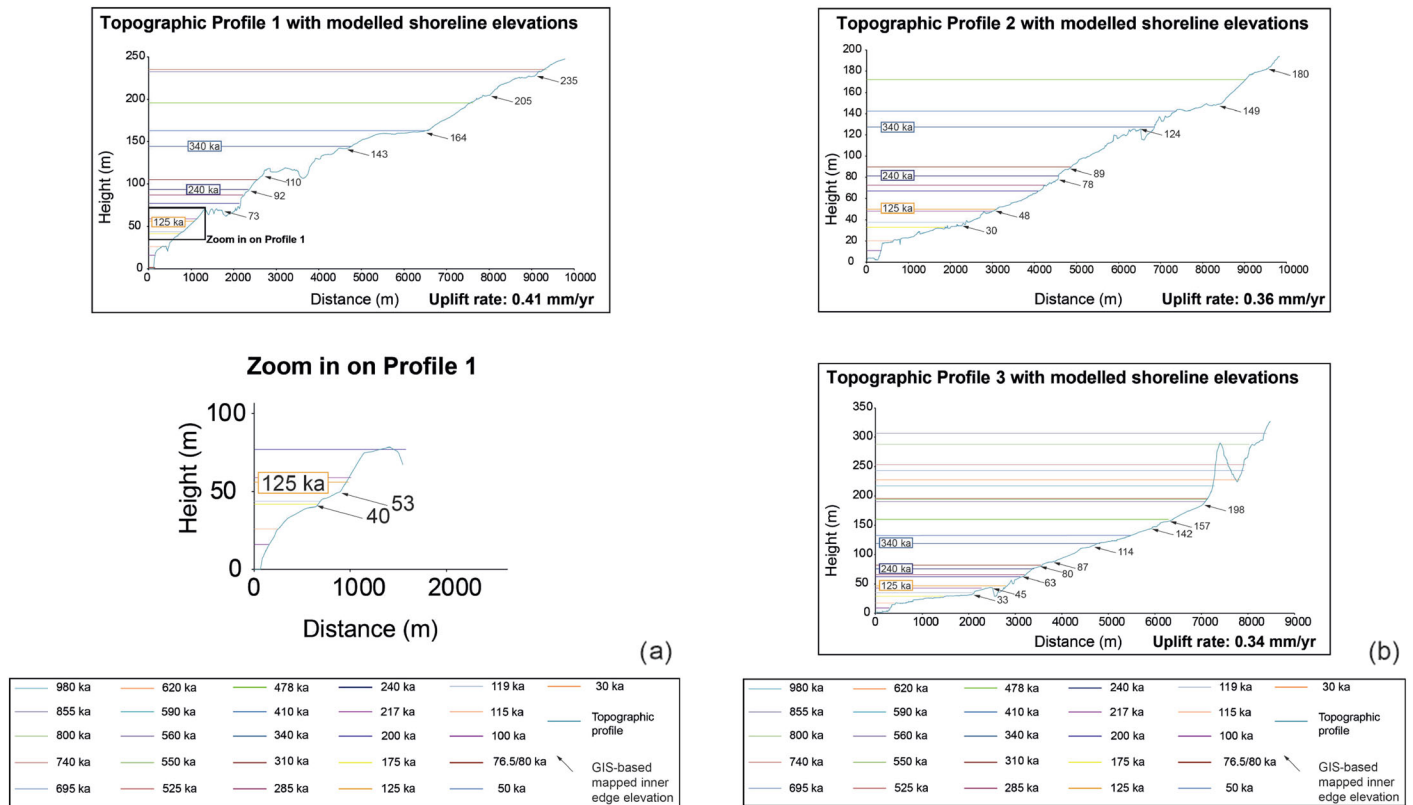


Figure 7a. Profiles showing mapped and modeled paleoshoreline elevations. The topographic profiles are from the 2 m DEM. The numbers with arrows mark the elevations of paleoshorelines mapped in the field. The colored lines indicate paleoshoreline elevations (or former sea level highstand elevations) predicted by an uplift rate that has been changed iteratively to produce the best match with the mapped paleoshorelines; goodness of fit is indicated by the value for the R^2 value in Figure 5 and RMS values in Figure 5. Profile locations shown in Figure 2.

not ruling out the possibility that the actual coral age could be 119 ka. We thus use this approximate age of 102 ka to further substantiate our results from synchronous correlation. In particular, the synchronous correlation approach applied along the Profile 11 suggests that the 14 m high terrace also mapped by Bianca et al. (1999) in the field with a previously proposed age of 60 ka must be older due to the existence of the approximate ~102 ka coral at this location. We are aware that our dated coral is not exactly at the elevation of the suggested sea level highstand (119 ka) but given the (i) uncertainty in the actual sea level curve ± 12 m for each sea level highstand from Siddall et al. (2003) and Rohling et al. (2014), the fact that corals do not live exactly at sea level and the unusually low $\delta^{234}\text{U}$ value this coral age is consistent with the interpretation of 119 ka sea level highstand. In summary, the three paleoshorelines can be explained with an uplift rate of 0.18 mm/yr, similar to that suggested by Dutton et al. (2009). Using this result as a guide, and by mapping the dated paleoshorelines from Profile 11 along strike, we then used synchronous correlation on other profiles across the terraces to study the spatial and temporal pattern of uplift.

Figure 7 shows our synchronous correlation between paleoshoreline elevations predicted by iterating values of uplift rate and paleoshoreline elevations mapped in the field and on DEMs. Two criteria were applied when we iterated the uplift rates driven by available age controls (Table 2) and supported by new coral dating (Table 3), and the results from Profile 11 (Figure 6): (i) we sought to ensure that the clearest mapped paleoshorelines were related to the most prominent sea level highstands at 125, 240, and 340 ka; (ii) we attempted to maximize the coefficient of determination (R^2) to demonstrate how robustly other less prominent mapped paleoshorelines match the iteratively predicted paleoshoreline elevations. This approach allows us to assign or in some cases reevaluate for the first-time ages for mapped, but undated paleoshorelines as shown in Table 4. To confirm that observations of the locations and elevations of paleoshorelines made on the DEMs were robust and consistent with field measurements, we have produced a cross plot

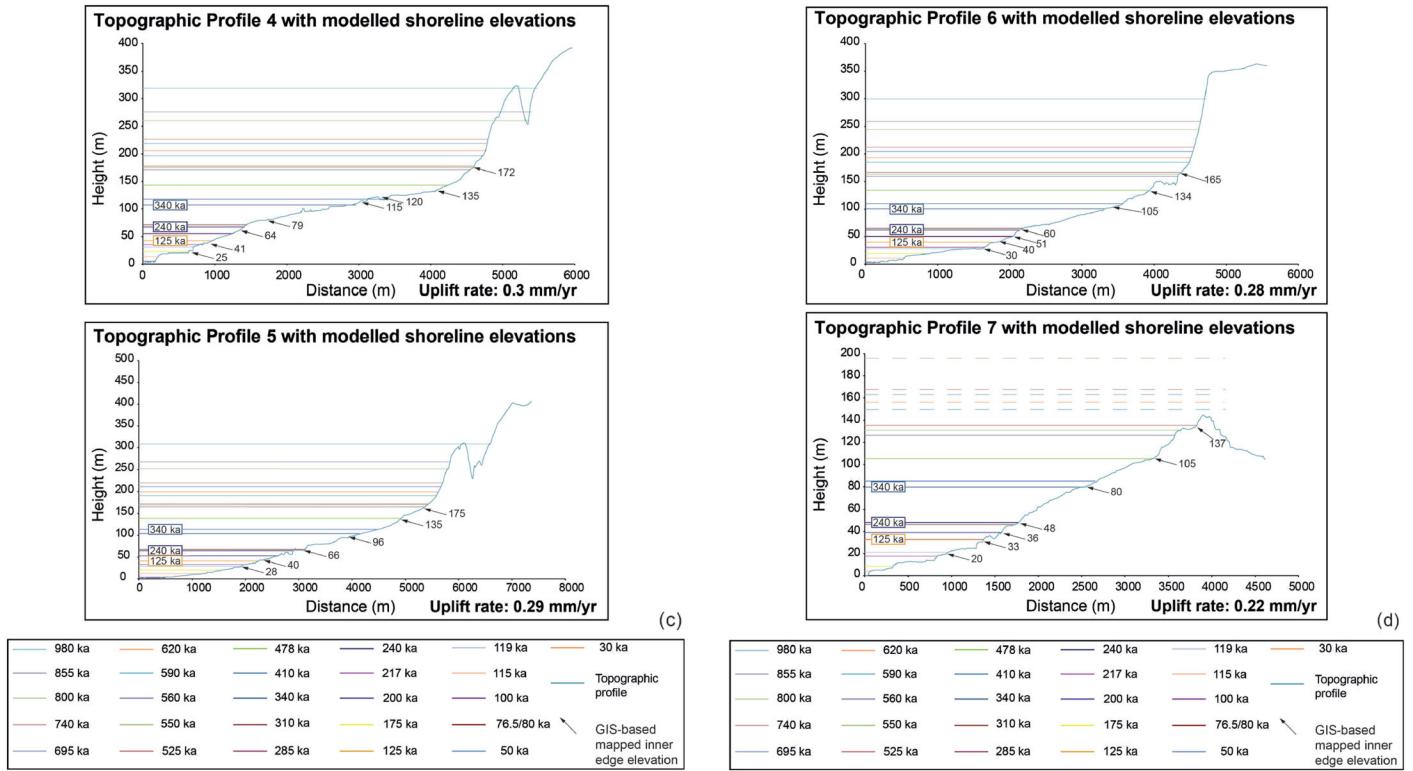


Figure 7b. (continued)

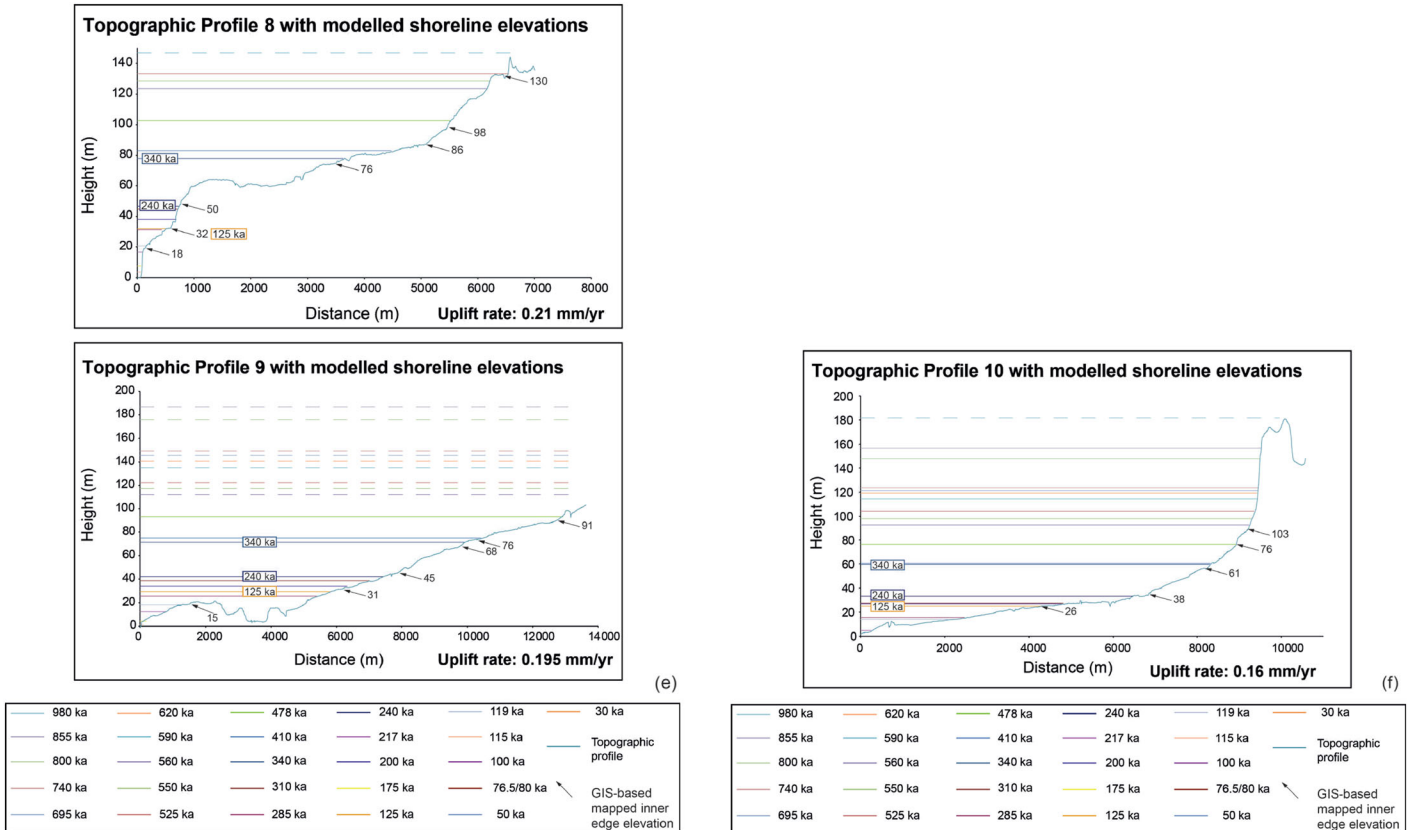


Figure 7c. (continued)

Table 4
All Mapped Inner Edges From DEM and Fieldwork With Age Assigned Via Synchronous Correlation Are Shown

Profile highstand Figure 2)	(sea level referred to)	UTM coordinate (easting)	UTM coordinate (northing)	DEMs elevations (m)	Expected elevations (m)	Our proposed age (kyr)	Age proposed by Bianca et al. (1999) (kyr)	Barometric altimeter paleoshoreline elevations (this study) (m)
1 (3a)		0511798	4128664	40	44	119	60	32
1 (3)		0511552	4128355	53	56	125	80	—
1 (5)		0510992	4127423	73	77	200	—	—
1 (7)		0510876	4127282	92	93	240	100	—
1 (9)		0510678	4127069	110	105	310	—	—
1 (10)		0509179	4125651	143	144	340	125	—
1 (11)		0507622	4124802	164	163	410	—	—
1 (12)		0506230	4124048	205	196	478	200	—
1 (13)		0505295	4123550	235	235	525	240	—
2 (3a)		0515345	4119964	30	38	119	60	—
2 (3)		0514217	4120518	48	50	125	80	—
2 (7)		0512863	4121361	78	81	240	100	—
2 (9)		0512577	4121369	89	90	310	—	—
2 (10)		0511095	4121342	124	127	340	125	—
2 (11)		0509086	4121288	149	143	410	—	—
2 (12)		0508187	4121081	180	172	478	200	—
3 (3a)		0514208	4118690	33	35	119	60	—
3 (3)		0513463	4118739	45	48	125	80	—
3 (5)		0512975	4118790	63	63	200	—	—
3 (7)		0512874	4118797	80	77	240	100	—
3 (9)		0512465	4118832	87	83	310	—	—
3 (10)		0511617	4118857	114	121	340	125	—
3 (11)		0510498	4118726	142	134	410	—	—
3 (12)		0509978	4118590	157	163	478	200	—
3 (13)		0509238	4118419	198	199	525	240	205
4 (3a)		0515954	4115491	25	31	119	60	—
4 (3)		0515706	4115434	41	43	125	80	—
4 (7)		0515298	4115351	64	67	240	100	—
4 (9)		0514853	4115267	79	71	310	—	—
4 (10)		0513649	4115181	115	107	340	125	—
4 (11)		0513067	4115071	120	118	410	—	—
4 (12)		0512748	4114826	135	143	478	200	—
4 (13)		0512365	4114546	172	178	525	240	—
3a (5)		0516074	4114009	28	30	119	60	—
3 (5)		0515745	4113944	40	41	125	80	—
7 (5)		0514956	4113539	66	65	240	100	—
10 (5)		0514144	4113529	96	104	340	125	—
12 (5)		0513225	4113844	135	139	478	200	133
13 (5)		0512742	4113972	175	172	525	240	180
6 (3a)		0516603	4112325	30	28	119	60	—
6 (3)		0516210	4111940	40	40	125	80	37
6 (5)		0516074	4111853	51	51	200	—	—
6 (7)		0515909	4111750	60	62	240	100	—
6 (10)		0514740	4111378	105	100	340	125	—
6 (12)		0514325	4111194	134	134	478	200	137
6 (13)		0513822	4110995	165	167	525	240	175
7 (3a)		0520284	4107458	20	21	119	60	—
7 (3)		0520014	4107098	33	33	125	80	34
7 (5)		0519936	4107052	36	39	200	—	—
7 (7)		0519682	4106913	48	48	240	100	50
7 (10)		0519037	4106554	80	80	340	125	87
7 (12)		0518482	4106306	105	105	478	200	102
7 (13)		0517809	4106154	137	136	525	240	134
8 (3a)		0526586	4105288	18	20	119	60	27
8 (3)		0526126	4105231	32	31	125	80	36
8 (7)		0525975	4105215	50	45	240	100	43
8 (10)		0523251	4104783	76	76	340	125	—
8 (11)		0521890	4104843	86	81	410	—	—

Table 4
Continued

Profile highstand Figure 2)	(sea level referred to)	UTM coordinate (easting)	UTM coordinate (northing)	DEMs elevations (m)	Expected elevations (m)	Our proposed age (kyr)	Age proposed by Bianca et al. (1999) (kyr)	Barometric altimeter paleoshoreline elevations (this study) (m)
8 (12)		0521306	4104935	98	100	478	200	91
8 (13)		0520334	4104971	130	130	525	240	139
9 (3a)		0523728	4098645	15	18	119	60	15
9 (3)		0518752	4098441	31	29	125	80	26
9 (7)		0517210	4099084	45	42	240	100	53
9 (10)		0515619	4099905	68	71	340	125	—
9 (11)		0514704	4100423	76	75	410	—	—
9 (12)		0513557	4101144	91	93	478	200	—
10 (3)		0519260	4094329	26	25	125	80	—
10 (7)		0517321	4095976	38	33	240	100	—
10 (10)		0516110	4096899	61	59	340	125	—
10 (12)		0515678	4096690	76	76	478	200	—
10 (13)		0515151	4096420	103	104	525	240	—
11 (3a)		0529880	4095212	14	16	119	60	14
11 (3)		0529261	4095438	27	28	125	80	27
11 (5)		0528919	4095511	32	31	200	—	—
11 (7)		0528518	4095580	38	38	240	100	40

Note. Note that all UTM coordinate are projected in 33°S grid zone. Note that not all the locations for inner edges mapped by DEMs analysis have been checked with GPS in the field because the investigated area is in places thickly vegetated and densely populated with private properties. However, see Figure 8 for a check of consistency between the two databases.

showing a linear regression analysis used to measure R^2 values, with a value of >0.99 , indicating a good correlation between paleoshorelines measured in the field and paleoshorelines measured on the DEMs. It is important to highlight that error bars on this linear regression analysis are assigned considering that DEMs used from “Regione Siciliana” have a 2 m resolution and paleoshoreline elevations mapped in the field have errors of ± 3 m associated with the handheld barometric altimeter. We checked the correlation between the DEMs-based topographic analysis and our mapped elevations in the field; we find that this correlation is robust within the margin of errors with $R^2 > 0.99$, suggesting that our “measured” elevations are reliable (Figure 8a). By linear regression analysis we assessed the robustness and reliability of the synchronous correlation approach between the “measured” paleoshoreline elevations in the field and DEMs and the “predicted” elevations iteratively calculated (Figure 8b), given (i) fixed values for sea level relative to today for several highstands presented by Siddall et al. (2003) and Rohling et al. (2014) (Table 1) and (ii) an uplift rate driven by ages constraints. This correlation with R^2 value >0.99 (Figure 8b) suggests that we have gained robust uplift rate estimates for the HP region, implying that the uplift rate has been constant through time for the last half million years. Our results also show that the locations of our mapped paleoshorelines are in very good agreement with those mapped by Bianca et al. (1999), yet, the suggested paleoshoreline ages in that study needed revision. Another important result, as already proposed by previous studies investigating uplifted paleoshorelines in the Mediterranean realm (Meschis et al., 2018; Roberts et al., 2013; Robertson et al., 2019), is that we have recognized and mapped paleoshorelines linked to the sea level highstands from 50, 76.5/80, 119, 125, 200, 240, 310, 340, 410, 478, and 525 ka (not all mapped within a single profile; Table 4). We stress that our refined chronology of paleoshoreline ages and associated uplift rates in this study agrees with independent and previous studies (Antonioli et al., 2006; Dutton et al., 2009) for the same region.

Our interpretation of paleoshorelines shows that uplift increases from south to north with tilted paleoshorelines (Figure 9a) over the Late Quaternary. Differential uplift rates (Figure 9b) are derived, with higher values of uplift rates mapped in the north (0.41 mm/yr), with lower values in the south (0.16 mm/yr). Furthermore, we have investigated whether the tilted geometry of mapped paleoshorelines developed sequentially through time or after all the terraces had been uplifted. If the tilting occurred gradually through time, older paleoshorelines would show higher values of tilt angle. Figure 9c shows that older and higher mapped paleoshorelines do indeed have higher values of tilt angle, suggesting that they have experienced

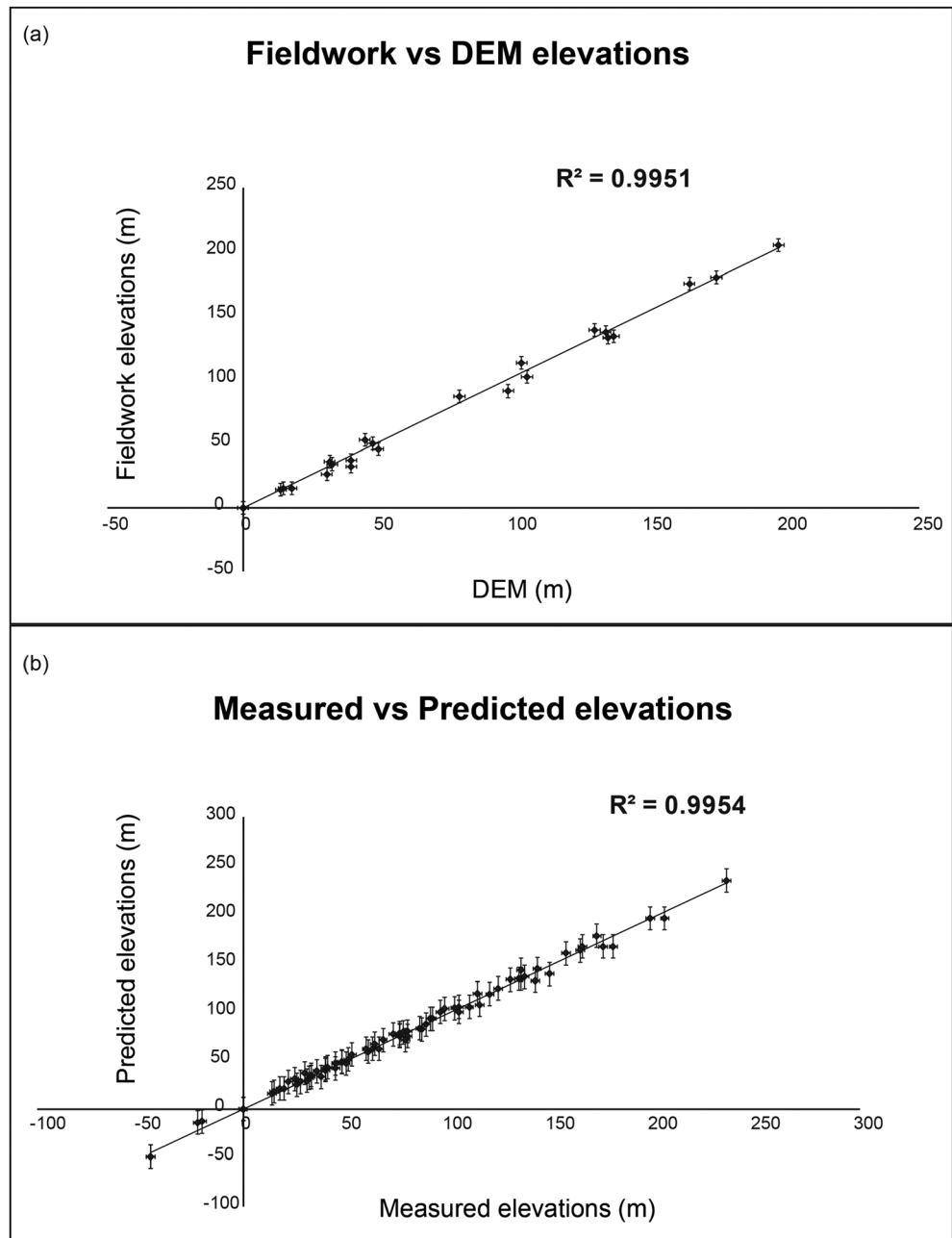
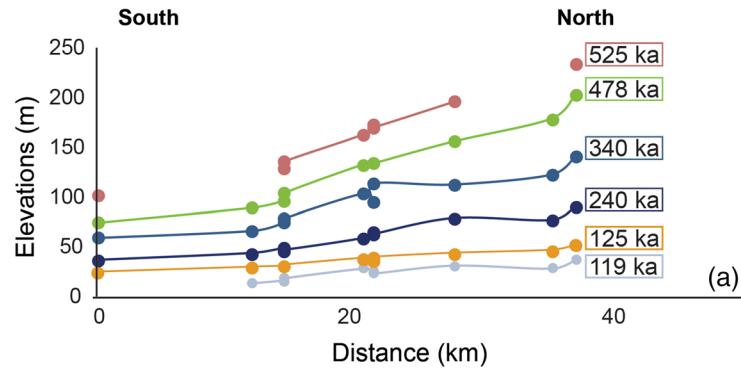


Figure 8. (a) Linear regression analysis shows the relationship between field-based and DEM-based inner edge elevation measurements. The R^2 value >0.99 confirms a strong correlation suggesting that elevations measured from the DEM are likely to be accurate. (b) Linear regression analysis between our measured and predicted paleoshoreline elevations. The predicted elevations, representing the synchronously calculated former sea level highstand elevations, indicate a constant uplift rate through time, that has been derived by iterating this value to find the best match to the measured and mapped paleoshorelines. Note that “measured” elevations represent paleoshoreline elevations mapped in the 2 m high resolution DEMs. Coefficient of determination, R^2 value, has been used between these two data sets to quantify the best fit for Profiles 1–10, with a value >0.99 .

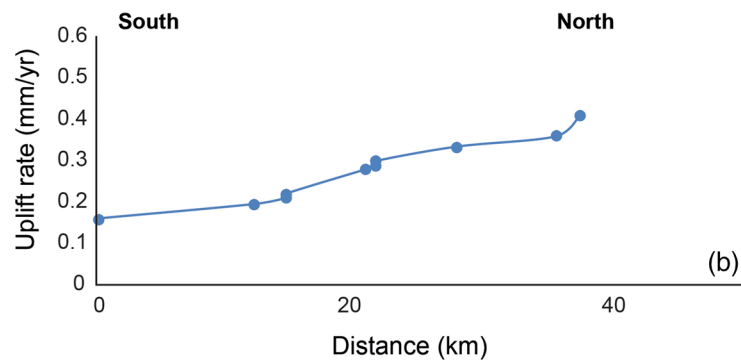
a longer history of differential uplift, and that tilting was ongoing through the Late Quaternary, and occurred progressively through time.

These interpretations showing differential uplift from north to south through time are in agreement with previous investigations for this area in terms of the locations and elevations of mapped paleoshorelines

Palaeoshoreline elevations along the Hyblean Plateau



Uplift rate along the Hyblean Plateau



Tilt angle vs Age

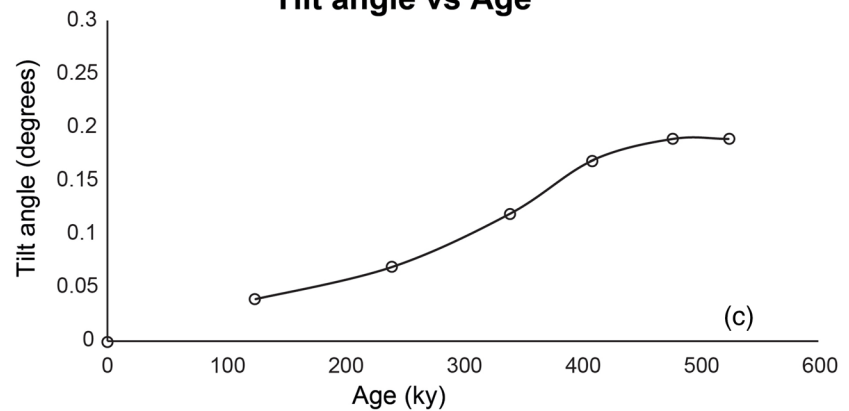


Figure 9. (a) Differential uplift from south to north of Late Quaternary paleoshorelines with paleoshoreline ages derived in this study. (b) Values for uplift rate increase from south to north along the N-S oriented transect. (c) Tilt angle values calculated for each mapped paleoshoreline in (a), showing that older paleoshorelines have higher tilt angles, suggesting that they have experienced a longer history of differential uplift and that differential uplift has been ongoing progressively during the Late Quaternary. Values of tilt angle for each investigated paleoshoreline have been calculated, as a \tan^{-1} of a gradient “ m ” of a straight-line equation ($y = mx$), as proposed by previous studies (Meschis et al., 2018; Robertson et al., 2019).

(Bianca et al., 1999; Ferranti et al., 2006; Spampinato et al., 2011). However, the paleoshorelines ages and hence uplift rates are not in agreement with these previous investigations.

In the next section, we discuss our results in terms of the relationships between the differential uplift we have mapped, and far-field geodynamic regional-scale processes and local “footwall uplift” produced by the activity of the offshore Western Fault.

5. Discussion

Our results suggest a constant uplift rate over the Late Quaternary, with the rate of uplift increasing from south to north (Figures 9a and 9b) within a foreland region represented by the HP. In this section we discuss possible mechanisms that may explain the Late Quaternary uplift of the HP. Finally, presented results will be briefly discussed in terms of seismic hazard affecting the SE Sicily.

5.1. Fluctuating Versus Constant Uplift Rate Through Time

By applying a synchronous correlation approach, we suggest that a constant uplift rate through time provides the best match between multiple paleoshorelines and multiple sea level highstands, and the limited age controls we have achieved with absolute dating (Figures 5–8). In other words, our best fit model achieves a close match to the geomorphology in terms of the elevations and number of paleoshorelines, but call into doubt the reliability of the 102 ka coral age, which in any case has an unusually low initial $\delta^{234}\text{U}$ value (Table 3). We suggest this coral age is a useful approximation, albeit with likely diagenetic alteration of the sample, that nonetheless suggests the “Siracusa-Terrace” is older than 60 ka, the value previously proposed (Bianca et al., 1999, yellow-colored terrace in their Figure 4). Indeed, our refined chronology, with a constant uplift rate through time, suggests that this terrace should belong to the minor peak of the LIM (119 ka) from north to south as shown in Figure 8 and Table 4. In this section, we briefly explore the possibility of using the potentially altered coral age as a more precise age constraint, but show that we prefer a model that emphasizes the good match between geomorphology and the model results over the reliability of the coral age. For instance, by applying our methodological approach on topographic Profile 1, driven by the calculated coral age, we would assign the MIS 5c (100 ka) age to the 40 m mapped paleoshoreline and claim a dramatic changing uplift rate through time (supporting information Figure S1). In particular, to find the best match between multiple paleoshoreline elevations and multiple sea level highstands, we would need to claim an uplift rate of 0.1 mm/yr before 100 ka and an uplift rate of 0.63 mm/yr after 100 ka. This would imply an unlikely uplift rate acceleration of $\times 6$ over a few 10,000 yr (supporting information Figure S2). Furthermore, this would also imply that one of the most common sea level highstand well recorded and mapped throughout the Mediterranean area like the MIS 7e (240 ka), at 92 m mapped along Profile 1 (Figure 7 and Table 4) in this study, (Meschis et al., 2018; Roberts et al., 2009, 2013; Robertson et al., 2019) would not be recorded because it would be overprinted by the higher and younger LIM (125 ka) (supporting information Figure S2a). Also, the RMS deviation, describing the best uplift rate value between the mapped geomorphology and the hypothesized model, calculated for this unlikely dramatic changing uplift rate scenario would be higher than the more likely “constant uplift rate” scenario claimed for this region. Because of the strong uncertainty affecting the calculated coral age due to the uncharacteristically low initial $\delta^{234}\text{U}$ value discussed in the previous section, we discard the dramatic “changing uplift rate” scenario for this area. We stress that in order to support an uplift rate acceleration, which would imply a drastic geodynamic change for the investigated area over a few 10,000 yr, more reliable data and perhaps different absolute dating techniques to gain new knowledge on paleoshoreline ages (e.g., Robertson et al., 2020) are needed. Thus, overall, we prefer an interpretation of the uplift as occurring at a constant rate because it provides a good match with the geomorphology, with a lower RMS value (4.21), and is a simpler case in terms of tectonic processes. Yet, still take account of the coral age in that we use it to call into doubt the existing published age of the 40 m terrace.

5.2. Multiple Components to Explain HP Uplift

According to previous works, uplift of the HP is due to footwall uplift over the Late Quaternary (Bianca et al., 1999; Monaco & Tortorici, 2000), and here we investigate whether offshore normal faults are close enough to the coast of the HP for this to be the case. It has been recognized that the effect of footwall uplift deformation decreases with distance from any given fault trace (DeMartini et al., 2004; Ward &

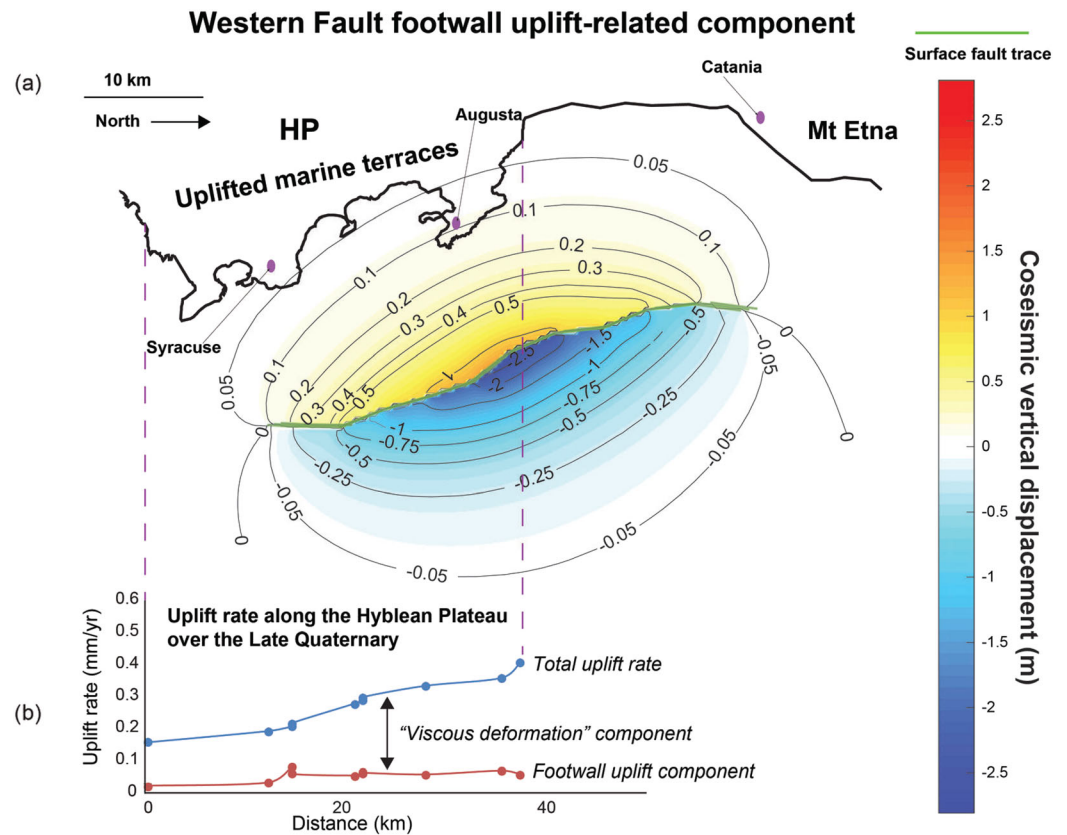


Figure 10. (a) Coseismic vertical displacements produced by the Western Fault suggested by half-elastic space modeling. The results indicate the extent to which footwall uplift affects the coastline of the Hyblean Plateau (HP). The model shows a simulated earthquake of $M_w 7.05$, produced if the entire length of the Western Fault (50 km) is ruptured with a slip at depth of 5.5 m, with a dip angle of 70° . (b) Assuming a recurrence interval of 500 yr, because shorter intervals are not supported by the historical earthquake record (see text for discussion of this value), the footwall uplift rate is <0.1 mm/yr, which does not explain the total uplift rate implied by our determinations based on the elevations of Late Quaternary palaeoshorelines. The discrepancy between uplift rates produced by footwall uplift and the total measured uplift rate is indicated (double-headed black arrow), and this may reveal the magnitudes of uplift rate produced by other processes.

Valensise, 1989). In particular, footwall uplift occurs for an across strike distance equal to about the half of the fault length. For instance, for the 1983 Borah Peak earthquake ($M_s 7.2$) on the Lost River Fault shows a coseismic surface rupture of ~ 30 km length and an associated footwall uplift deformation of ~ 15 km into the footwall measured from its maximum displacement at the fault center (Stein & Barrientos, 1985). Similarly, for the L'Aquila earthquake ($M_w 6.2$) the Paganica Fault produced a coseismic surface rupture of ~ 24 km, with an associated footwall uplift deformation of ~ 12 km into the footwall measured from its maximum displacement at the fault center (Papanikolaou et al., 2010). The most damaging and powerful earthquake recorded in Europe produced by a normal fault, namely the Messina-Taormina Fault, shows a coseismic rupture of ~ 58 km with an associated footwall uplift deformation of ~ 29 km into the footwall modeled from its maximum displacement at the fault center (Meschis et al., 2019). Offshore of the investigated area, crustal extension accommodated by the east dipping Western Fault (Argnani et al., 2012; Argnani & Bonazzi, 2005; Bianca et al., 1999) presents an entire length of ~ 50 km and is mapped between 14 and 20 km offshore of the investigated area. From the above, we would expect footwall uplift to extend 25 km into the footwall if the entire fault length ruptures. To test this, and quantify the magnitude of expected uplift, we modeled slip on the offshore mapped Western Fault in an elastic half-space using the Coulomb 3.4 software (Toda et al., 2011), applying a new Matlab code (Mildon et al., 2016) that allows us to include the mapped curvilinear fault trace and hence likely corrugated geometry of the fault plane. These combined codes allow us to model vertical and horizontal crustal movement produced by earthquakes on faults showing variable-strike geometry (Iezzi et al., 2018; Mildon et al., 2016; Toda et al., 2011), such as the coseismic

Continental convergence-related crustal thickening component

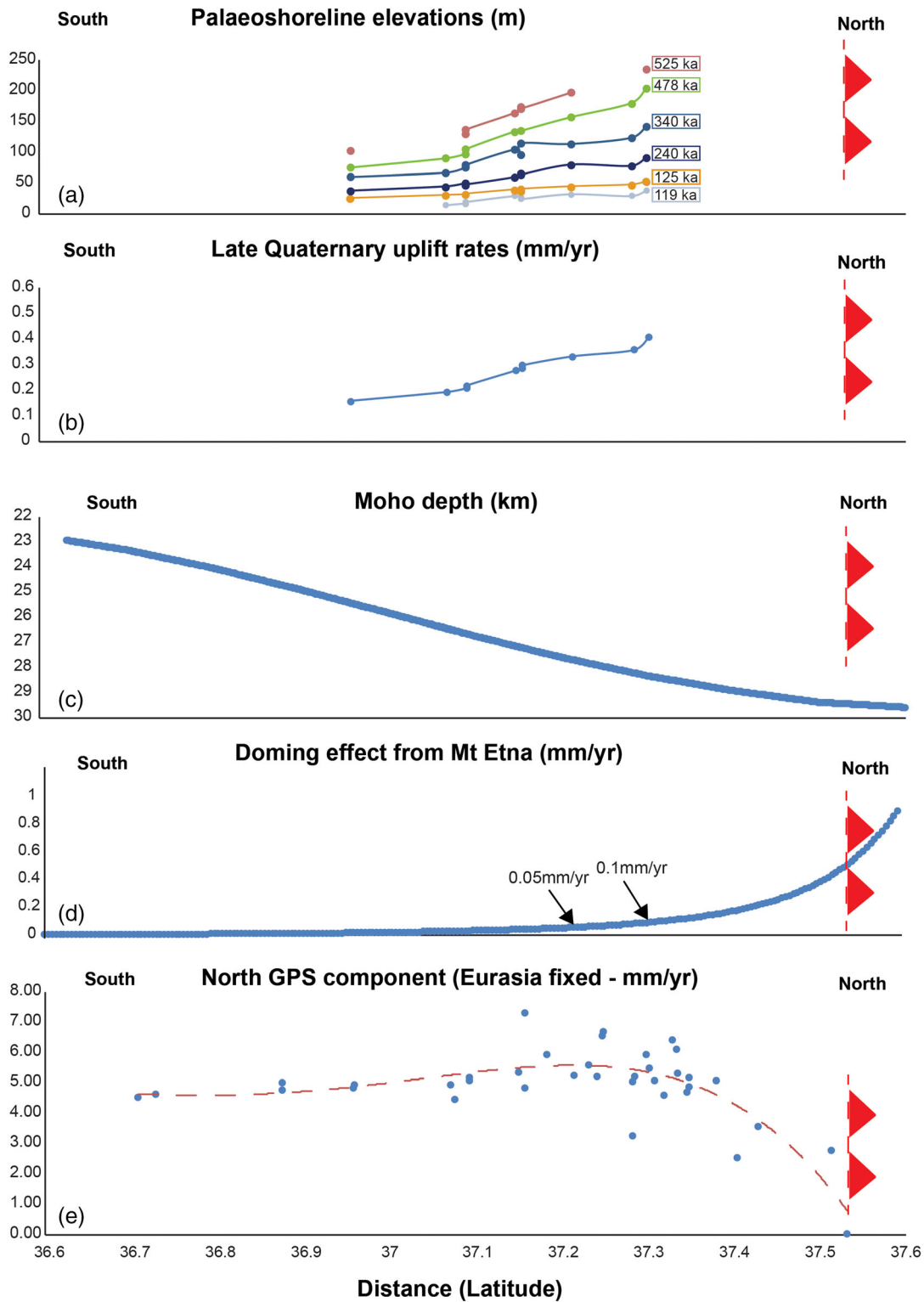


Figure 11. Uplift rates obtained results from this paper (a, b) shown in the context of crustal thickening (c), the doming effects related to Etna (d), and horizontal GPS velocities (e). Higher values of uplift (a) and uplift rates (b) develop toward the north where deeper values of Moho discontinuity are mapped (c), higher values for uplift related to Etna (d), and lower values of horizontal GPS velocities approaching the thrust on the north side of the HP (e).

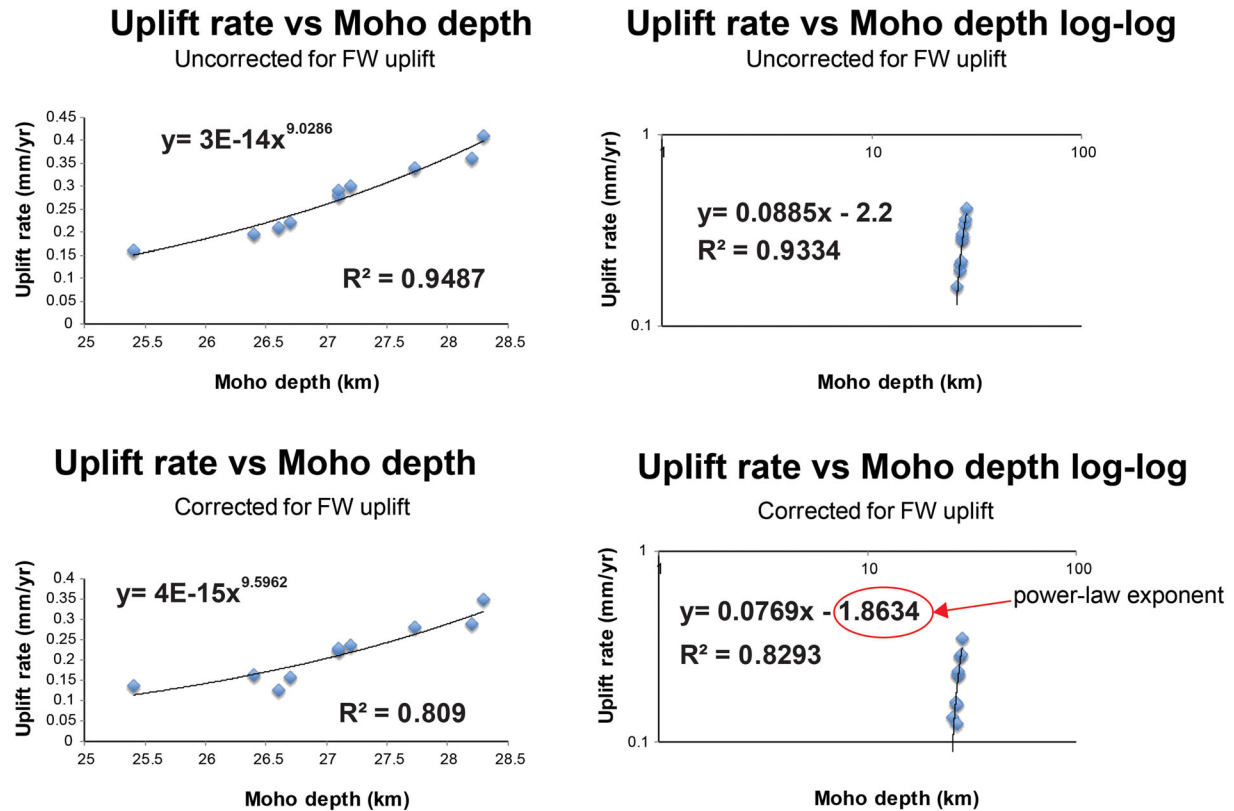


Figure 12. The relationship between uplift rate and Moho depth. Regression analysis of values for uplift rate and Moho depth reveal a power law relationship with an exponent of 1.86. This suggests that viscous deformation may be associated with the measured deformation.

uplift and subsidence adjacent to the investigated fault (Figure 10). For this paper, we used fault parameters of a 50 km-long east dipping fault with a dip angle of 70° (Bianca et al., 1999) and slip at depth of 5.5 m, at 5 km depth, with 10% of the slip maximum propagating to the surface, in order to obtain an earthquake magnitude of $\sim M_w$ 7.05. We also did the same with a fault dip of 30°. Our modeling reveals that a 70° dip angle produces coseismic footwall uplift affecting the eastern HP where uplifted paleoshorelines are mapped (Figure 10a). A dip angle of 30° produces quasi-zero uplift of the coast and hence was not investigated further (see supporting information Figure S3). Furthermore, using the 70° dip angle, we calculated the uplift rate of the coastline, assuming the slip rate and hence uplift rate are constant over the last 525,000 yr, by assuming a recurrence interval of 500 yr, as previously proposed by some (Bianca et al., 1999). This recurrence interval of 500 yr is likely to be close to a minimum plausible value, as more frequent recurrence would be recorded in the historical record and this is not the case (Guidoboni et al., 2007). The graph presented in Figure 10b shows that the long-term footwall uplift effect produces uplift rates that peak on the coast opposite the center of the offshore fault but decreasing to the north and south. Thus, this does not explain the uplift increasing to the north, as described earlier in this paper. Furthermore, footwall uplift would produce only small part of the total magnitude of the uplift constrained by the uplifted paleoshorelines given the earthquake recurrence interval we have assumed as a minimum value; additional uplift is required suggesting the existence of multiple processes contributing to the uplift.

Other explanations of uplift within NE Sicily and Calabria since Middle Pleistocene have been related to the Ionian subduction-collision and back-arc spreading processes associated mantle flow around southeastward retreating Ionian slab (Barreca et al., 2016; Faccenna et al., 2004, 2011; Lucente et al., 2006; Scarfi et al., 2018) alongside isostatic rebound in response to slab detachment (Gvirtzman & Nur, 1999; Neri et al., 2012; Westaway, 1993). We noted that uplift and uplift rates measured in this paper (Figures 11a and 11b) show higher values where higher depth values of the Moho discontinuity are mapped (Figure 11c). Moreover,

recent geophysical investigations of the lithosphere show that slab detachment and mantle flow also occur north of the HP. Assuming that the effect of these processes vanishes toward the south, the correlation between deep-seated subcrustal processes and observed differential uplift could be consistent with the uplift mapped by Ferranti et al. (2006) and that mapped in this paper. Indeed, we note that Figure 12 shows a non-linear correlation between uplift rate and Moho depth with a power law exponent of ~ 1.86 . This may suggest that viscous deformation is an important process in this area, because the relationship resembles that for viscous flow where driving stress raised to an exponent relates to the strain rate (Cowie et al., 2013; Hirth et al., 2001; Shi et al., 2015). This may be related to viscous crustal or mantle flow due to slab processes or crustal thickening. Modeling to differentiate between these viscous processes is beyond the scope of this paper, but, in summary, we suggest for the first time, that viscous processes combined with the offshore Western Fault footwall uplift may control the uplift of the HP (Figures 10 and 11). Interestingly, similar combined mechanisms (regional processes and local contribution from faults) to explain crustal uplift, constrained by investigating raised paleoshorelines, have been proposed for northern Calabria (Italy) (Santoro et al., 2013).

Finally, it can be argued that the crustal uplift in the northern rim of the HP could also be affected by the deep magmatic processes associated with the Etna volcano; however, taking into account the long-term magmatic source with the associated “doming effect” suggested by De Guidi et al. (2014), it is likely that the “doming effect” only provides a fraction of the total measured uplift (Figure 11d).

5.3. Long-Term Seismic Implications and Future Investigations

We now turn to the question of whether we can use the uplift rates we have described to help identify potential seismic sources.

Our discussion above suggests that normal faulting and associated footwall uplift could contribute to the measured uplift through the Quaternary. If the constant Quaternary uplift rate suggests a constant slip rate through time on the offshore normal fault this may produce new insights into its associated seismic hazard. To gain actual values for the slip rate on the normal fault one would have to subtract any uplift produced by regional processes. Otherwise, erroneous fault slip rates and earthquake recurrence intervals will be derived for long-term seismic hazard assessment. This will be crucial if we consider that this fault (i) can produce damaging earthquakes with $\sim M_w 7$ if the entire fault length is ruptured and (ii) cannot be ruled out as the seismogenic source of the 1693 “Val di Noto” earthquake ($M 7.4$). We, although, highlight that because the dominant signal of the uplift is from regional processes, we are aware that any possible small fluctuation on the slip rate of the Western Fault over the Quaternary can have been overwhelmed by them. We stress that more investigations are needed to refine deformation rates associated to the Western Fault.

Also, it is important to highlight that the differential uplift we describe may well have been active through the Holocene. Vertical deformation studies within the HP have shown that higher Holocene uplift rates have been mapped close to Augusta town and the northern rim of the HP, and lower values have been mapped in the south around the location of Profile 10 (Scicchitano et al., 2008, 2017; Spampinato et al., 2011) (Holocene uplift rates increase from 0.24 to 0.74 mm/yr from south to north; Figure 1). Moreover, a similar uplift gradient from north to south is recorded by GPS-based vertical movement investigations (Serpelloni et al., 2013). Although more detailed studies which cover the Holocene to present time are needed, this may suggest that the ongoing Africa-Eurasia convergence (Figure 11e) and the offshore extensional Western Fault are seismically active processes that combine to produce constant rates through time, implying that more investigations are needed for a better (i) understanding of their relationship and (ii) seismic hazard approach.

6. Conclusions

In this paper, we use the synchronous correlation technique as methodological approach in order to refine ages for undated marine terraces. This allows us to refine uplift rates through time, overcoming the “overprinting problem” when we investigate regions affected by relatively low uplift rates such as the HP, SE Sicily. New rates of uplift constant through time spanning the Late Quaternary have been presented within the investigated area. By applying the synchronous correlation approach, driven by new age controls, a sequence of uplifted Late Quaternary marine terraces has been investigated. It has been shown

that (i) paleoshoreline elevations increase from south to north, (ii) higher uplift rates are mapped in the northern rim of the HP, and (iii) their tilt angle shows higher values for the older and higher terraces. This suggests that regional geodynamics and long-term activity of the offshore Western Fault were the combined cause of uplift and have been constant through time. This highlights new insights for the long-term seismic hazard approach for one of the most seismically active regions in the Mediterranean Basin.

Data Availability Statement

All data for this paper are properly cited and referred to in the reference list and available in Figure 7, as topographic data where paleoshoreline elevations have been mapped, and in Table 4 (all mapped paleoshoreline elevations and assigned ages). These data can be used to reproduce all results shown in Figures 8 and 9. The data are stored online (at <https://doi.org/10.17632/v252gjjg782.1>). Moho depth shown on Figure 11 have been derived from <https://www.seismo.helsinki.fi/mohomap/>, with related publications properly cited in the Reference list. They are also available by contacting the corresponding author (marco.meschis.14@ucl.ac.uk, marco.meschis@gmail.com).

Acknowledgments

We thank Prof. Jonathan Aitchison, the Associate Editor, Luigi Ferranti, and an anonymous reviewer for critically improving this manuscript with their comments. This work was funded and supported by the London NERC DTP Scholarship (grant number reference: 1492238). $^{234}\text{U}/^{230}\text{Th}$ coral age dating was carried out at the Geochronology and Tracers Facility (BGS, UK) via Grant IP-1734-0517. We thank “Regione Siciliana” for helping us to access the 2 m Digital Elevation Models. Dr. Mimmo Palano is thanked for providing the “Etna Doming Effect” data shown in Figure 11.

References

- Aloisi, M., Bruno, V., Cannavo, F., Ferranti, L., Mattia, M., & Monaco, C. (2013). Are the source models of the *M* 7.1 1908 Messina Straits earthquake reliable? Insights from a novel inversion and sensitivity analysis of levelling data by Aloisi et al. (2012). *Geophysical Journal International*, *192*, 1025–1041. <https://doi.org/10.1093/gji/ggs062>
- Anderson, R. S., Densmore, A. L., & Ellis, M. A. (1999). The generation and degradation of marine terraces. *Basin Research*, *11*(1), 7–19. <https://doi.org/10.1046/j.1365-2117.1999.00085.x>
- Antonoli, F., Kershaw, S., Renda, P., Rust, D., Belluomini, G., Cerasoli, M., et al. (2006). Elevation of the last interglacial highstand in Sicily (Italy): A benchmark of coastal tectonics. *Quaternary International*, *145–146*, 3–18. <https://doi.org/10.1016/j.quaint.2005.07.002>
- Argnani, A., Armigliato, A., Pagnoni, G., Zaniboni, F., Tinti, S., & Bonazzi, C. (2012). Active tectonics along the submarine slope of south-eastern Sicily and the source of the 11 January 1693 earthquake and tsunami. *Natural Hazards and Earth System Sciences*, *2010*, 1311–1319. <https://doi.org/10.5194/nhess-12-1311-2012>
- Argnani, A., & Bonazzi, C. (2005). Malta escarpment fault zone offshore eastern Sicily: Pliocene-Quaternary tectonic evolution based on new multichannel seismic data. *Tectonics*, *24*, TC4009. <https://doi.org/10.1029/2004TC001656>
- Armijo, R., Meyer, B., King, G. C. P., Rigo, A., & Papanastassiou, D. (1996). Quaternary evolution of the Corinth Rift and its implications for the late Cenozoic evolution of the Aegean. *Geophysical Journal International*, *126*(1), 11–53. <https://doi.org/10.1111/j.1365-246X.1996.tb05264.x>
- Azzaro, R., & Barbano, M. S. (2000). Analysis of the seismicity of southeastern Sicily: A proposed tectonic interpretation. *Annali di Geofisica*, *43*(1), 171–188.
- Barreca, G., Scarfi, L., Cannavò, F., Koulakov, I., & Monaco, C. (2016). New structural and seismological evidence and interpretation of a lithospheric-scale shear zone at the southern edge of the Ionian subduction system (central-eastern Sicily, Italy). *Tectonics*, *35*, 1489–1505. <https://doi.org/10.1002/2015TC004057>
- Ben-Avraham, Z., & Grasso, M. (1991). Crustal structure variations and transcurrent faulting at the eastern and western margins of the eastern Mediterranean. *Tectonophysics*, *196*(3–4), 269–277. [https://doi.org/10.1016/0040-1951\(91\)90326-N](https://doi.org/10.1016/0040-1951(91)90326-N)
- Bianca, M., Monaco, C., Tortorici, L., & Cernobori, L. (1999). Quaternary normal faulting in southeastern Sicily (Italy): A seismic source for the 1693 large earthquake. *Geophysical Journal International*, *139*(2), 370–394. <https://doi.org/10.1046/j.1365-246x.1999.00942.x>
- Billi, A., Porreca, M., Faccenna, C., & Mattei, M. (2006). Magnetic and structural constraints for the noncylindrical evolution of a continental forebulge (Hyblea, Italy). *Tectonics*, *25*, TC3011. <https://doi.org/10.1029/2005TC001800>
- Burrollet, P. F., Mugniot, J. M., & Sweeney, P. (1978). The geology of the Pelagian block: The margins and basins off southern Tunisia and Tripolitania. In *The ocean basins and margins* (pp. 331–359). Boston, MA: Springer US. https://doi.org/10.1007/978-1-4684-3039-4_6
- Caputo, R., Bianca, M., & D’Onofrio, R. (2010). Ionian marine terraces of southern Italy: Insights into the Quaternary tectonic evolution of the area. *Tectonics*, *29*, TC4005. <https://doi.org/10.1029/2009TC002625>
- Catalano, R., Doglioni, C., & Merlini, S. (2001). On the Mesozoic Ionian Basin. *Geophysical Journal International*, *144*(1), 49–64. <https://doi.org/10.1046/j.0956-540X.2000.01287.x>
- Cheng, H., Lawrence Edwards, R., Shen, C. C., Polyak, V. J., Asmerom, Y., Woodhead, J., et al. (2013). Improvements in ^{230}Th dating, ^{230}Th and ^{234}U half-life values, and U–Th isotopic measurements by multi-collector inductively coupled plasma mass spectrometry. *Earth and Planetary Science Letters*, *371–372*, 82–91. <https://doi.org/10.1016/j.epsl.2013.04.006>
- Chiapparba, C., & Palano, M. (2017). Progressive migration of slab break-off along the southern Tyrrhenian plate boundary: Constraints for the present day kinematics. *Journal of Geodynamics*, *105*, 51–61. <https://doi.org/10.1016/j.jog.2017.01.006>
- Cogan, J., Rigo, L., Grasso, M., & Lerche, I. (1989). Flexural tectonics of southeastern Sicily. *Journal of Geodynamics*, *11*(3), 189–241. [https://doi.org/10.1016/0264-3707\(89\)90007-0](https://doi.org/10.1016/0264-3707(89)90007-0)
- Cowie, P. a., Scholz, C. H., Roberts, G. P., Faure Walker, J. P., & Steer, P. (2013). Viscous roots of active seismogenic faults revealed by geologic slip rate variations. *Nature Geoscience*, *6*(12), 1036–1040. <https://doi.org/10.1038/ngeo1991>
- Crémère, A., Lepland, A., Chand, S., Sahy, D., Condon, D. J., Noble, S. R., et al. (2016). Timescales of methane seepage on the Norwegian margin following collapse of the Scandinavian ice sheet. *Nature Communications*, *7*(1), 11509. <https://doi.org/10.1038/ncomms11509>
- Cultrera, F., Barreca, G., Scarfi, L., & Monaco, C. (2015). Fault reactivation by stress pattern reorganization in the Hyblean foreland domain of SE Sicily (Italy) and seismotectonic implications. *Tectonophysics*, *661*, 215–228. <https://doi.org/10.1016/j.tecto.2015.08.043>
- Cutler, K. B., Edwards, R. L., Taylor, F. W., Cheng, H., Adkins, J., Gallup, C. D., et al. (2003). Rapid sea-level fall and deep-ocean temperature change since the last interglacial period. *Earth and Planetary Science Letters*, *206*(3–4), 253–271. [https://doi.org/10.1016/S0012-821X\(02\)01107-X](https://doi.org/10.1016/S0012-821X(02)01107-X)

- De Guidi, G., Barberi, G., Barreca, G., Bruno, V., Cultrera, F., Grassi, S., et al. (2015). Geological, seismological and geodetic evidence of active thrusting and folding south of Mt. Etna (eastern Sicily): Reevaluation of "seismic efficiency" of the Sicilian basal thrust. *Journal of Geodynamics*, 90, 32–41. <https://doi.org/10.1016/j.jog.2015.06.001>
- De Guidi, G., Imposa, S., Scudero, S., & Palano, M. (2014). New evidence for Late Quaternary deformation of the substratum of Mt. Etna volcano (Sicily, Italy): Clues indicate active crustal doming. *Bulletin of Volcanology*, 76(5), 1–13. <https://doi.org/10.1007/s00445-014-0816-8>
- Dellong, D., Klingelhoefer, F., Dannowski, A., Kopp, H., Murphy, S., Graindorge, D., et al. (2020). Geometry of the deep Calabrian subduction (central Mediterranean Sea) from wide-angle seismic data and 3-D gravity modeling. *Geochemistry, Geophysics, Geosystems*, 21(3). <https://doi.org/10.1029/2019GC008586>
- Dellong, D., Klingelhoefer, F., Kopp, H., Graindorge, D., Margheriti, L., Moretti, M., et al. (2018). Crustal structure of the Ionian Basin and eastern Sicily margin: Results from a wide-angle seismic survey. *Journal of Geophysical Research: Solid Earth*, 123, 2090–2114. <https://doi.org/10.1002/2017JB015312>
- DeMartini, P. M., Pantosti, D., Palyvos, N., Lemeille, F., McNeill, L., & Collier, R. (2004). Slip rates of the Aigion and Eliki faults from uplifted marine terraces, Corinth Gulf, Greece. *Comptes Rendus Geoscience*, 336(4–5), 325–334. <https://doi.org/10.1016/j.crte.2003.12.006>
- DeMets, C., Iaffaldano, G., & Merkouriev, S. (2015). High-resolution Neogene and Quaternary estimates of Nubia-Eurasia-North America plate motion. *Geophysical Journal International*, 203(1), 416–427. <https://doi.org/10.1093/gji/ggv277>
- Dewey, J. F., Helman, M. L., Knott, S. D., Turco, E., & Hutton, D. H. W. (1989). Kinematics of the western Mediterranean. *Geological Society, London, Special Publications*, 45(1), 265–283. <https://doi.org/10.1144/GSL.SP.1989.045.01.15>
- Drysdale, R. N., Hellstrom, J. C., Zanchetta, G., Fallick, A. E., Sanchez Goni, M. F., Couchoud, I., et al. (2009). Evidence for obliquity forcing of glacial termination II. *Science*, 325(5947), 1527–1531. <https://doi.org/10.1126/science.1170371>
- Dutton, A. (2015). Uranium-thorium dating. In *Handbook of sea-level research* (pp. 386–403). Chichester, UK: John Wiley & Sons, Ltd. <https://doi.org/10.1002/9781118452547.ch26>
- Dutton, A., Scicchitano, G., Monaco, C., Desmarchelier, J. M., Antonioli, F., Lambeck, K., et al. (2009). Uplift rates defined by U-series and ¹⁴C ages of serpulid-encrusted speleothems from submerged caves near Siracusa, Sicily (Italy). *Quaternary Geochronology*, 4(1), 2–10. <https://doi.org/10.1016/j.quageo.2008.06.003>
- El-Asmar, H. (1997). Quaternary isotope stratigraphy and paleoclimate of coral reef terraces, Gulf of Aqaba, South Sinai, Egypt. *Quaternary Science Reviews*, 16(8), 911–924. [https://doi.org/10.1016/S0277-3791\(96\)00077-7](https://doi.org/10.1016/S0277-3791(96)00077-7)
- Faccenna, C., Funicello, F., Giardini, D., & Lucente, P. (2001). Episodic back-arc extension during restricted mantle convection in the central Mediterranean. *Earth and Planetary Science Letters*, 187(1–2), 105–116. [https://doi.org/10.1016/S0012-821X\(01\)00280-1](https://doi.org/10.1016/S0012-821X(01)00280-1)
- Faccenna, C., Molin, P., Orecchio, B., Olivetti, V., Bellier, O., Funicello, F., et al. (2011). Topography of the Calabria subduction zone (southern Italy): Clues for the origin of Mt. Etna. *Tectonics*, 30, TC1003. <https://doi.org/10.1029/2010TC002694>
- Faccenna, C., Piromallo, C., Crespo-Blanc, A., Jolivet, L., & Rossetti, F. (2004). Lateral slab deformation and the origin of the western Mediterranean arcs. *Tectonics*, 23, TC1012. <https://doi.org/10.1029/2002TC001488>
- Ferranti, L., Antonioli, F., Mauz, B., Amorosi, A., Dai Pra, G., Mastronuzzi, G., et al. (2006). Markers of the last interglacial sea-level high stand along the coast of Italy: Tectonic implications. *Quaternary International*, 145–146, 30–54. <https://doi.org/10.1016/j.quaint.2005.07.009>
- Ferranti, L., Monaco, C., Antonioli, F., Maschio, L., Kershaw, S., & Verrubbi, V. (2007). The contribution of regional uplift and coseismic slip to the vertical crustal motion in the Messina Straits, southern Italy: Evidence from raised Late Holocene shorelines. *Journal of Geophysical Research*, 112, B06401. <https://doi.org/10.1029/2006JB004473>
- Ferranti, L., Oldow, J. S., D'Argenio, B., Catalano, R., Lewis, D., Marsella, E., et al. (2008). Active deformation in southern Italy, Sicily and southern Sardinia from GPS velocities of the Peri-Tyrrhenian Geodetic Array (PTGA). *Bollettino della Società Geologica Italiana*, 127(2), 299–316.
- Firth, C., & Stewart, I. (1996). Coastal elevation changes in eastern Sicily: Implications for volcano instability at Mount Etna. *Geological Society, London, Special Publications*, 110, 153–167. <https://doi.org/10.1144/GSL.SP.1996.110.01.12>
- Ford, D., & Williams, P. (2007). *Karst hydrogeology and geomorphology*. West Sussex, England: John Wiley & Sons Ltd. <https://doi.org/10.1002/9781118684986>
- Gallen, S. F., Wegmann, K. W., Bohnenstiehl, D. R., Pazzaglia, F. J., Brandon, M. T., & Fassoulas, C. (2014). Active simultaneous uplift and margin-normal extension in a forearc high, Crete, Greece. *Earth and Planetary Science Letters*, 398, 11–24. <https://doi.org/10.1016/j.epsl.2014.04.038>
- Gascoyne, M., Ford, D., & Schwarz, H. (1983). Rates of cave and landform development in the Yorkshire Dales from speleothem age data. *Earth Surface Processes and Landforms*, 8, 557–568.
- Giunta, G., Gueli, A. M., Monaco, C., Orioli, S., Ristuccia, G. M., Stella, G., & Troja, S. O. (2012). Middle-Late Pleistocene marine terraces and fault activity in the Sant'Agata di Militello coastal area (north-eastern Sicily). *Journal of Geodynamics*, 55, 32–40. <https://doi.org/10.1016/j.jog.2011.11.005>
- Goede, A., & Vogel, J. C. (1991). Trace element variations and dating of a Late Pleistocene Tasmanian speleothem. *Palaeogeography, Palaeoclimatology, Palaeoecology*, 88, 121–131.
- Grad, M., & Taira, T. (2009). The Moho depth map of the European plate. *Geophysical Journal International*, 176(1), 279–292. <https://doi.org/10.1111/j.1365-246X.2008.03919.x>
- Grasso, M., & Lentini, F. (1982). Sedimentary and tectonic evolution of the eastern Hyblean Plateau (southeastern Sicily) during late Cretaceous to Quaternary time. *Palaeogeography, Palaeoclimatology, Palaeoecology*, 39(3–4), 261–280. [https://doi.org/10.1016/0031-0182\(82\)90025-6](https://doi.org/10.1016/0031-0182(82)90025-6)
- Grasso, M., Miuccio, G., Maniscalco, R., Garofalo, P., La Manna, F., & Stamilla, R. (1995). Plio-Pleistocene structural evolution of the western margin of the Hyblean Plateau and the Maghrebian foredeep, SE Sicily. Implications for the deformational history of the Gela Nappe. *Annales Tectonicae*, 9, 7–21.
- Guidoboni, E., Ferrari, G., Mariotti, D., Comastri, A., Tarabusi, G., & Valensise, G. (2007). Catalogue of strong earthquakes in Italy (461 BC–1997) and Mediterranean area (760 BC–1500). Available from <http://storing.ingv.it/cfti4med/>
- Gutscher, M.-A., Roger, J., Baptista, M.-A., Miranda, J. M., & Tinti, S. (2006). Source of the 1693 Catania earthquake and tsunamis (southern Italy): New evidence from tsunami modeling of a locked subduction fault plane. *Geophysical Research Letters*, 33, L08309. <https://doi.org/10.1029/2005GL025442>
- Gvirtzman, Z., & Nur, A. (1999). Plate detachment, asthenosphere upwelling, and topography across subduction zones. *Geology*, 27(6), 563. [https://doi.org/10.1130/0091-7613\(1999\)027<0563:PDAUAT>2.3.CO;2](https://doi.org/10.1130/0091-7613(1999)027<0563:PDAUAT>2.3.CO;2)

- Gvirtzman, Z., & Nur, A. (2001). Residual topography, lithospheric structure and sunken slabs in the central Mediterranean. *Earth and Planetary Science Letters*, 187(1–2), 117–130. [https://doi.org/10.1016/S0012-821X\(01\)00272-2](https://doi.org/10.1016/S0012-821X(01)00272-2)
- Hirth, G., Teyssier, C., & Dunlap, J. W. (2001). An evaluation of quartzite flow laws based on comparisons between experimentally and naturally deformed rocks. *International Journal of Earth Sciences*, 90(1), 77–87. <https://doi.org/10.1007/s005310000152>
- Hirn, A., Nicolich, R., Gallart, J., Laigle, M., Cernobori, L., & ETNASEIS Scientific Group (1997). Roots of Etna volcano in faults of great earthquakes. *Earth and Planetary Science Letters*, 148(1–2), 171–191. [https://doi.org/10.1016/S0012-821X\(97\)00023-x](https://doi.org/10.1016/S0012-821X(97)00023-x)
- Houghton, S. L., Roberts, G. P., Papanikolaou, I. D., & McArthur, J. M. (2003). New ²³⁴U–²³⁰Th coral dates from the western Gulf of Corinth: Implications for extensional tectonics. *Geophysical Research Letters*, 30(19), 2013. <https://doi.org/10.1029/2003GL018112>
- Iezzi, F., Mildon, Z., Walker, J. F., Roberts, G., Goodall, H., Wilkinson, M., & Robertson, J. (2018). Coseismic throw variation across along-strike bends on active normal faults: Implications for displacement versus length scaling of earthquake ruptures. *Journal of Geophysical Research: Solid Earth*, 123, 9817–9841. <https://doi.org/10.1029/2018JB016732>
- INGV - DISS Working Group. (2018). Database of Individual Seismogenic Sources (DISS), Version 3.2.1: A compilation of potential sources for earthquakes larger than M 5.5 in Italy and surrounding areas. <https://doi.org/10.6092/INGV.IT-DISS3.2.1>
- Jacques, E., Monaco, C., Tapponnier, P., Tortorici, L., & Winter, T. (2001). Faulting and earthquake triggering during the 1783 Calabria seismic sequence. *Geophysical Journal International*, 147(3), 499–516. <https://doi.org/10.1046/j.0956-540x.2001.01518.x>
- Lajoie, K. R. (1986). Coastal tectonics. In *Active tectonics: Impact on society* (pp. 95–124). Retrieved from <http://books.google.com/books?hl=en&lr=&id=qaz9KnE2lxQC&pgis=1>
- Lavecchia, G., Ferrarini, F., de Nardis, R., Visini, F., & Barbano, M. S. (2007). Active thrusting as a possible seismogenic source in Sicily (southern Italy): Some insights from integrated structural–kinematic and seismological data. *Tectonophysics*, 445(3–4), 145–167. <https://doi.org/10.1016/j.tecto.2007.07.007>
- Lentini, F., Di Geronimo, I., Grasso, M., Carbone, S., Sciuto, F., Scamarda, G., et al. (1987). Carta geologica della Sicilia sud-orientale. Università di Catania, Istituto di Scienze della Terra, 1987. S.EL.CA. Ed, Florence.
- Lucente, F. P., Margheriti, L., Piromallo, C., & Barrool, G. (2006). Seismic anisotropy reveals the long route of the slab through the western-central Mediterranean mantle. *Earth and Planetary Science Letters*, 241(3–4), 517–529. <https://doi.org/10.1016/j.epsl.2005.10.041>
- Mastrolobo Ventura, B., Serpelloni, E., Argnani, A., Bonforte, A., Bürgmann, R., Anzidei, M., et al. (2014). Fast geodetic strain-rates in eastern Sicily (southern Italy): New insights into block tectonics and seismic potential in the area of the great 1693 earthquake. *Earth and Planetary Science Letters*, 404, 77–88. <https://doi.org/10.1016/j.epsl.2014.07.025>
- Mattia, M., Bruno, V., Cannavò, F., & Palano, M. (2012). Evidences of a contractional pattern along the northern rim of the Hyblean Plateau (Sicily, Italy) from GPS data. *Geologica Acta*, 10(1), 63–70. <https://doi.org/10.1344/105.000001705>
- Meschis, M., Roberts, G. P., Mildon, Z. K., Robertson, J., Michetti, A. M., & Faure Walker, J. P. (2019). Slip on a mapped normal fault for the 28th December 1908 Messina earthquake (Mw 7.1) in Italy. *Scientific Reports*, 9, 1–8. <https://doi.org/10.1038/s41598-019-42915-2>
- Meschis, M., Roberts, G. P., Robertson, J., & Briant, R. M. (2018). The relationships between regional Quaternary uplift, deformation across active Normal faults, and historical seismicity in the upper plate of subduction zones: The Capo D'Orlando fault, NE Sicily. *Tectonics*, 37, 1231–1255. <https://doi.org/10.1029/2017TC004705>
- Mickler, P. J., Stern, L. A., Banner, J. L., Cave, H., & Only, W. I. (2006). Large kinetic isotope effects in modern speleothems. *GSA Bulletin*, 118(1–2), 65–81. <https://doi.org/10.1130/B25698.1>
- Mildon, Z. K., Toda, S., Faure Walker, J. P., & Roberts, G. P. (2016). Evaluating models of Coulomb stress transfer: Is variable fault geometry important? *Geophysical Research Letters*, 43, 12,407–12,414. <https://doi.org/10.1002/2016GL071128>
- Miller, W. R., & Mason, T. R. (1994). Erosional features of coastal beachrock and aeolianite outcrops in Natal and Zululand, South Africa. *Journal of Coastal Research*, 10(2), 374–394. <https://doi.org/10.2307/4298223>
- Monaco, C., Bianca, M., Catalano, S., Guidi, D., & Tortorici, L. (2002). Sudden change in the Late Quaternary tectonic regime in eastern Sicily: Evidences from geological and geomorphological features. *Bollettino della Società Geologica Italiana*, 1(January), 901–913.
- Monaco, C., & Tortorici, L. (2000). Active faulting in the Calabrian Arc and eastern Sicily. *Journal of Geodynamics*, 29(3–5), 407–424. [https://doi.org/10.1016/S0264-3707\(99\)00052-6](https://doi.org/10.1016/S0264-3707(99)00052-6)
- Musgrove, M., Banner, J. L., Mack, L. E., Combs, D. M., James, E. W., & Edwards, R. L. (2001). Geochronology of late Pleistocene to Holocene speleothems from central Texas: Implications for regional paleoclimate. *Geological Society of America Bulletin*, 113(12), 1532–1543. [https://doi.org/10.1130/0016-7606\(2001\)113<1532:GOLPTH>2.0.CO;2](https://doi.org/10.1130/0016-7606(2001)113<1532:GOLPTH>2.0.CO;2)
- Musumeci, C., Scarfi, L., Palano, M., & Patanè, D. (2014). Foreland segmentation along an active convergent margin: New constraints in southeastern Sicily (Italy) from seismic and geodetic observations. *Tectonophysics*, 630, 137–149. <https://doi.org/10.1016/j.tecto.2014.05.017>
- Neri, G., Barberi, G., Orecchio, B., & Aloisi, M. (2002). Seismotomography of the crust in the transition zone between the southern Tyrrhenian and Sicilian tectonic domains. *Geophysical Research Letters*, 29(23), 2135. <https://doi.org/10.1029/2002GL015562>
- Neri, G., Marotta, A. M., Orecchio, B., Presti, D., & Tortorici, L. (2012). How lithospheric subduction changes along the Calabrian Arc in southern Italy: Geophysical evidences. *International Journal of Earth Sciences*, 101(7), 1949–1969. <https://doi.org/10.1007/s00531-012-0762-7>
- Nicolich, R., Laigle, M., Hirn, A., Cernobori, L., & Gallart, J. (2000). Crustal structure of the Ionian margin of Sicily: Etna volcano in the frame of regional evolution. *Tectonophysics*, 329(1–4), 121–139. [https://doi.org/10.1016/S0040-1951\(00\)00192-X](https://doi.org/10.1016/S0040-1951(00)00192-X)
- Niggemann, S., Mangini, A., Richter, D. K., & Wurth, G. (2003). A paleoclimate record of the last 17,600 years in stalagmites from the B7 cave, Sauerland, Germany. *Quaternary Science Reviews*, 22(5–7), 555–567.
- Palano, M., Ferranti, L., Monaco, C., Mattia, M., Aloisi, M., Bruno, V., et al. (2012). GPS velocity and strain fields in Sicily and southern Calabria, Italy: Updated geodetic constraints on tectonic block interaction in the central Mediterranean. *Rendiconti Online della Società Geologica Italiana*, 117(B7), 235–237. <https://doi.org/10.1029/2012JB009254>
- Papanikolaou, I. D., Foumelis, M., Parcharidis, I., Lekkas, E. L., & Fountoulis, I. G. (2010). Deformation pattern of the 6 and 7 April 2009, MW = 6.3 and MW = 5.6 earthquakes in L'Aquila (Central Italy) revealed by ground and space based observations. *Natural Hazards and Earth System Sciences*, 10, 73–87. <https://doi.org/10.5194/nhess-10-73-2010>
- Pedley, M. H., & Grasso, M. (1992). Miocene syntectonic sedimentation along the western margins of the Hyblean-Malta platform: A guide to plate margin processes in the central Mediterranean. *Journal of Geodynamics*, 15(1–2), 19–37. [https://doi.org/10.1016/0264-3707\(92\)90004-C](https://doi.org/10.1016/0264-3707(92)90004-C)
- Pedoja, K., Jara-Muñoz, J., de Gelder, G., Robertson, J., Meschis, M., Fernandez-Blanco, D., et al. (2018). Neogene-Quaternary slow coastal uplift of Western Europe through the perspective of sequences of strandlines from the Cotentin Peninsula (Normandy, France). *Geomorphology*, 303, 338–356. <https://doi.org/10.1016/j.geomorph.2017.11.021>

- Piatanesi, A., & Tinti, S. (1998). A revision of the 1693 eastern Sicily earthquake and tsunamis. *Journal of Geophysical Research*, *103*(B2), 2749–2758. <https://doi.org/10.1029/97JB03403>
- Roberts, G. P., Houghton, S. L., Underwood, C., Papanikolaou, I., Cowie, P. A., van Calsteren, P., et al. (2009). Localization of Quaternary slip rates in an active rift in 10 5 years: An example from central Greece constrained by ^{234}U - ^{230}Th coral dates from uplifted paleoshorelines. *Journal of Geophysical Research*, *114*, B10406. <https://doi.org/10.1029/2008JB005818>
- Roberts, G. P., Meschis, M., Houghton, S., Underwood, C., & Briant, R. M. (2013). The implications of revised Quaternary palaeoshoreline chronologies for the rates of active extension and uplift in the upper plate of subduction zones. *Quaternary Science Reviews*, *78*, 169–187. <https://doi.org/10.1016/j.quascirev.2013.08.006>
- Robertson, J., Meschis, M., Roberts, G. P., Ganas, A., & Gheorghiu, D. (2019). Temporally constant Quaternary uplift rates and their relationship with extensional upper-plate faults in south Crete (Greece), constrained with ^{36}Cl cosmogenic exposure dating. *Tectonics*, *38*, 1189–1222. <https://doi.org/10.1029/2018TC005410>
- Robertson, J., Roberts, G. P., Iezzi, F., Meschis, M., Gheorghiu, D. M., Sahy, D., et al. (2020). Distributed normal faulting in the tip zone of the south Alkyonides fault system, Gulf of Corinth, constrained using ^{36}Cl exposure dating of late-Quaternary wave-cut platforms. *Journal of Structural Geology*, *136*(April), 104063. <https://doi.org/10.1016/j.jsg.2020.104063>
- Rohling, E. J., Foster, G. L., Grant, K. M., Marino, G., Roberts, A. P., Tamisiea, M. E., & Williams, F. (2014). Sea-level and deep-sea-temperature variability over the past 5.3 million years. *Nature*, *508*(7497), 477–482. <https://doi.org/10.1038/nature13230>
- Rowe, P. J., Wickens, L. B., Sahy, D., Marca, A. D., Peckover, E., Noble, S., et al. (2020). Multi-proxy speleothem record of climate instability during the early last interglacial in southern Turkey. *Palaeogeography, Palaeoclimatology, Palaeoecology*, *538*, 109422. <https://doi.org/10.1016/j.palaeo.2019.109422>
- Santoro, E., Ferranti, L., Burrato, P., Mazzella, M. E., & Monaco, C. (2013). Deformed Pleistocene marine terraces along the Ionian Sea margin of southern Italy: Unveiling blind fault-related folds contribution to coastal uplift. *Tectonics*, *32*, 737–762. <https://doi.org/10.1002/tect.20036>
- Scarfi, L., Barberi, G., Barreca, G., Cannavò, F., Koulakov, I., & Patanè, D. (2018). Slab narrowing in the central Mediterranean: The Calabro-Ionian subduction zone as imaged by high resolution seismic tomography. *Scientific Reports*, *8*(1), 5178. <https://doi.org/10.1038/s41598-018-23543-8>
- Scicchitano, G., Berlinghieri, E. F. C., Antonioli, F., Spampinato, C. R., & Monaco, C. (2017). Sacred landscapes and changing sea levels: New interdisciplinary data from the early Neolithic to the present in south-eastern Sicily. In *Under the Sea: Archaeology and Palaeolandscapes of the Continental Shelf* (pp. 233–253). https://doi.org/10.1007/978-3-319-53160-1_16
- Scicchitano, G., Antonioli, F., Berlinghieri, E. F. C., Dutton, A., & Monaco, C. (2008). Submerged archaeological sites along the Ionian coast of southeastern Sicily (Italy) and implications for the Holocene relative sea-level change. *Quaternary Research*, *70*(1), 26–39. <https://doi.org/10.1016/j.yqres.2008.03.008>
- Sengör, A. M. C. (1979). Mid-Mesozoic closure of Permo-Triassic Tethys and its implications. *Nature*, *279*(5714), 590–593. <https://doi.org/10.1038/279590a0>
- Serpelloni, E., Faccenna, C., Spada, G., Dong, D., & Williams, S. D. P. (2013). Vertical GPS ground motion rates in the Euro-Mediterranean region: New evidence of velocity gradients at different spatial scales along the Nubia-Eurasia plate boundary. *Journal of Geophysical Research: Solid Earth*, *118*, 6003–6024. <https://doi.org/10.1002/2013JB010102>
- Shi, F., Zhang, J., Xia, G., Jin, Z., & Green, H. W. (2015). Rheology of Mg_2GeO_4 olivine and spinel harzburgite: Implications for Earth's mantle transition zone. *Geophysical Research Letters*, *42*, 2212–2218. <https://doi.org/10.1002/2015GL063316>
- Siddall, M., Rohling, E. J., Almogi-Labin, A., Hemleben, C., Meischner, D., Schmelzer, I., & Smeed, D. A. (2003). Sea-level fluctuations during the last glacial cycle. *Nature*, *423*(6942), 853–858. <https://doi.org/10.1038/nature01690>
- Spampinato, C. R., Costa, B., Di Stefano, A., Monaco, C., & Scicchitano, G. (2011). The contribution of tectonics to relative sea-level change during the Holocene in coastal south-eastern Sicily: New data from boreholes. *Quaternary International*, *232*(1–2), 214–227. <https://doi.org/10.1016/j.quaint.2010.06.025>
- Stein, R. S., & Barrientos, S. E. (1985). Planar high-angle faulting in the basin and range: Geodetic analysis of the 1983 Borah Peak, Idaho, earthquake. *Journal of Geophysical Research*, *90*(B13), 11355. <https://doi.org/10.1029/JB090iB13p11355>
- Toda, S., Stein, R. S., Sevilgen, V., & Lin, J. (2011). Coulomb 3.3. Graphic-rich deformation & stress-change software for earthquake, tectonic and volcano research and teaching—User guide. *USGS Open-File Report*, 63. Retrieved from <https://pubs.usgs.gov/of/2011/1060/>
- Torelli, L., Grasso, M., Mazzoldi, G., & Peis, D. (1998). Plio-Quaternary tectonic evolution and structure of the Catania foredeep, the northern Hyblean Plateau and the Ionian shelf (SE Sicily). *Tectonophysics*, *298*(1–3), 209–221. [https://doi.org/10.1016/S0040-1951\(98\)00185-1](https://doi.org/10.1016/S0040-1951(98)00185-1)
- Tortorici, G., De Guidi, G., & Sturiale, G. (2006). Evoluzione tettonica quaternaria del margine settentrionale del Plateau Ibleo (Sicilia sud-orientale). *Bollettino della Società Geologica Italiana*, *125*(1), 21–37.
- Waelbroeck, C., Labeyrie, L., Michel, E., Duplessy, J. C., McManus, J. F., Lambeck, K., et al. (2002). Sea-level and deep water temperature changes derived from benthic foraminifera isotopic records. *Quaternary Science Reviews*, *21*(1–3), 295–305. [https://doi.org/10.1016/S0277-3791\(01\)00101-9](https://doi.org/10.1016/S0277-3791(01)00101-9)
- Ward, S. N., & Valensise, G. (1989). Fault parameters and slip distribution of the 1915 Avezzano, Italy, earthquake derived from geodetic observations. *Bulletin of the Seismological Society of America*, *79*(3), 690–710.
- Wells, D. L., & Coppersmith, K. J. (1994). New empirical relationships among magnitude, rupture length, rupture width, rupture area, and surface displacement. *Bulletin of the Seismological Society of America*, *84*(4), 974–1002. Retrieved from <http://www.bssaonline.org/content/84/4/974.short>
- Westaway, R. (1993). Quaternary uplift of southern Italy. *Journal of Geophysical Research*, *98*(B12), 741–772. <https://doi.org/10.1029/93JB01566>